Data assimilation in thermoacoustic instability with Lagrangian optimization

Traverso Tullio

DIME

Università degli studi di Genova

This dissertation is submitted for the degree of

Master in Mechanical Engineering, Energy and Aeronautics

Magri L., Bottaro A.   October 2018

Dedico questa tesi a tutte le persone che si sono prese il rischio di darmi fiducia.

Acknowledgements

Ringrazio il mio supervisore di Cambridge, Luca Magri, per avermi proposto un lavoro interessante e soprattutto per come mi ha guidato durante il suo svolgimento. Lo ha fatto consapevole, e forse ancora memore, di come ci si sente quando, per la prima volta, si prova a fare della ricerca scientifica. E' in questo frangente che la figura del supervisore gioca uno dei ruoli più importanti e delicati.

Ringrazio il mio supervisore di Genova, Alessandro Bottaro, per l'opportunità che mi ha dato e la fiducia che ha sempre dimostrato nei miei confronti. "...Lei pensi ad andare a Cambridge e a farsi valere..." è stato l'inizio, e ho cercato di tenerlo presente. Ringrazio entrambi per il tempo che mi hanno dedicato nella scelta del dottorato, dandomi preziosi consigli e condividedndo opinioni esperte.

Ringrazio i miei genitori, mio fratello e mia zia, per essermi stati sempre vicino e per avermi permesso, prima di chiunque altro, di vivere questa lunga e articolata esperienza di studio, durata due decenni.

Ringrazio quello che è nato come il mio gruppo di studio, Gotte, Fillo, Edo e Giuli, con cui ho superato tutti gli esami più difficili. Hanno rappresentato, in innumerevoli occasioni, la sola ragione per alzarsi la mattina e andare studiare. Senza di loro, una qualche tesi col mio nome sopra apparirebbe solo tra qualche anno.

Ringrazio, Ema, Fabri, Lore, Matte, Rachele, Ste e Vale per il loro sostegno morale e materiale. Per essere stati ad ogni aeroporto e stazione da cui io sia partito o arrivato, per ricordarmi che credono in me e che mi pensano. Facendomi sentire parte di una seconda famiglia.

Abstract

Two-way coupling between acoustic pressure oscillations and the unsteady heat released by the flame in a combustion chamber can result in thermoacoustic instabilities. Low-order models can only qualitatively predict such instabilities. In order to make low-order models quantitatively predictive, we apply data assimilation for parameter and state estimation. We numerically extract information about the most likely estimate of the model state using the 4D-Var data assimilation technique on a Galerkin discretised time-delayed model of a model combustor. Data assimilation is an optimal blending of observations with previous system's state estimate (background) to produce optimal initial conditions. The model realisation associated with the optimal initial conditions is called analysis. A cost functional is defined to measure (i) the statistical distance between the model output and the measurements from experiments and (ii) the distance between the model's initial conditions and the background knowledge. Its minimum corresponds to the optimal state, which is obtained by Lagrangian optimization with the aid of adjoint equations. First, we study the influence of the number of Galerkin modes, which are the natural acoustic modes of the duct, with which the adjoint equations are discretised. We show that decomposing the measured pressure signal in a finite number of modes is an effective way to enhance the state estimation, especially when highly nonlinear modal interactions occur in the assimilation window. Secondly, we reveal that there is a threshold value for the number of measurements, based on their accuracy, above which no useful information is added to the analysis. The effect of the assimilation window length on the Analysis solution is thoroughly investigated. To the best of the author's knowledge, this work represents the first application of Data Assimilation to thermoacoustic instability. It opens up new possibilities for realtime calibration of low-order models with experimental

measurements.

Indice

Capitolo 1

Introduction

Introduction

Many gas turbine combustion systems suffer from large-amplitude velocity and pressure acoustic oscillations [1]. These self-excited oscillations occur due to the coupling between unsteady heat release and acoustic waves in confined spaces that can lead to resonance [1]. Unsteady combustion is an efficient source of acoustic waves and the boundaries of a combustor are acoustically closed and have little acoustic dissipation [2]. Therefore acoustic waves are reflected at the boundaries and they propagate back to the combustion zone perturbing the flame, which results in fluctuating heat release and further generation of acoustic waves. When the acoustic pressure fluctuations and the unsteady heat release are sufficiently in phase, the acoustic waves may be amplified [1; 3]. In gas turbine combustion systems the amplification can be very severe because of the large energy density and small acoustic dissipation. This results in increased emissions, a deterioration in the performance of the gas turbine system, flame blowoff or flashback, high heat transfer rates and highly energetic vibrations resulting in the damage of the combustion chamber [1]. Modern gas turbines operate under lean premixed conditions in order to lower NOx emissions by lowering the temperature in the combustion zone. Operating under lean premixed conditions, however, makes gas turbines highly susceptible to thermoacoustic oscillations [4]. Preventing these oscillations by avoiding operating conditions where they occur or controlling them to stay

below acceptable amplitudes, therefore, is of great importance to gas turbine manufacturers. Thermoacoustic oscillations are one of the most challenging problems in gas turbine technology. Thermoacoustic oscillations may be controlled by either passive or active means [5]. Passive control uses damping mechanisms, such as Helmholtz resonators or perforated plates, to dissipate some of the acoustic energy or modification of the combustion system to alter time delays, combustor geometry or flame stabilization regions [1]. The use of passive control is constrained by the geometries of combustors and the limited range of frequencies over which passive control devices are effective. Active control aims to modify the feedback between the acoustics and the flame so that thermoacoustic oscillations decay [1]. Active control uses actuation that provides external energy to the system, and can be further divided into open-loop and closed-loop active control [6]. Open-loop active control does not use sensors for feedback and the forcing (actuation) does not depend on the measurement of any physical quantity [6]. Closed-loop active control uses sensors to measure physical quantities, controllers to determine the signal required to alter the feedback between the unsteady heat release and acoustics based on the input signal from the sensors, and actuators to alter some physical quantity based on the signal from the controller [7]. The limited accuracy and reliability of sensors in the turbulent environment of combustors, and the limited speed, bandwidth and amplitude of actuators, however, makes their use difficult. Controller design is challenging because of large time delays, the noisy environment of combustors and the existence of multiple unstable modes [8; 9]. Active control of combustion oscillations remains an active area of research [1; 5; 10]. Both designing controllers and finding regions of safe operation of the system require good understanding of the dynamics of the system. The dynamics of the system depends broadly on two types of physical processes: (i) the feedback between the flame and the acoustics, which is responsible for feeding energy into the oscillations, and (ii) the damping within the system and at its boundaries, which is responsible for dissipating energy. The mechanisms involved in the interaction between the flame and the acoustics include hydrodynamic instabilities, gas dynamics, chemical reactions, heat transfer, multi-phase flows etc. Importantly, these mechanisms are not confined to the vicinity of the combustion zone [11]. They include a range of length scales because acoustic waves

propagate much faster than the mean flow (in gas turbines) and boundaries far upstream or downstream of the combustion zone can affect the dynamics of the system. Likewise, hydrodynamic instabilities initiated in the injector cause perturbations that advect downstream at convection speeds of the order of the mean flow. When these arrive at the flame, they perturb the flame surface causing heat release rate fluctuations far downstream of the region of absolute instability [46]. The mechanisms involved in dissipating energy include viscous and thermal losses in boundary layers, radiation of acoustic energy, and the interactions between acoustic waves, entropy waves and vorticity [12]. Therefore, understanding the underlying mechanisms that couple the unsteady heat release rate from flames and acoustic waves is a challenging task. The mechanisms responsible for driving thermoacoustic oscillations in gas turbine combustors and the interactions between these mechanisms, as well as those that cause damping, were reviewed by Candel [10], Lieuwen [13] and Huang and Yang [14]. Besides understanding the mechanisms, the nature of these oscillations (e.g. periodic, quasi-periodic, chaotic) ought to be understood to predict when they are likely to occur, how operating conditions should be changed to avoid their occurrence and whether they can be triggered by noise in the system. The onset of these oscillations is well understood using linear theories [3; 15; 16; 17]. However, the transient behaviour, the ultimate state reached by the system, and the susceptibility to triggering, which all depend on its thermoacoustic nonlinear behaviour, are poorly understood.

1.1   Nonlinear thermoacoustics

Thermoacoustics has been studied for over five decades. This field was actively researched during the 1960s and 70s because it was a persistent problem in rocket motors with liquid and solid propellants [18]. There has been renewed interest recently, incorporating research from nonlinear dynamics from the 1970s and 80s, a knowledge that was not available to researchers in the 1960s and 70s.

1.1.1 Source of nonlinearity in thermoacoustics

In rocket motors, the pressure perturbations are comparable to the mean pressure, therefore nonlinearities in the acoustics are important. Formation of weak shock waves is common [18; 19]. Culick [20] derived an analytical expression for the existence and stability of limit cycles using second-order nonlinear gas dynamics. Subsequent studies considered other types of nonlinearity, including nonlinearities in the heat release rate response to velocity perturbations [21]. In gas turbine systems, however, the pressure perturbations are small compared to the mean pressure and the velocity perturbations are small compared to the speed of sound. Furthermore, the mean flow is small compared to the speed of sound. Therefore second and higher order terms involving the mean flow Mach number and perturbation Mach number in the nonlinear gas dynamic equations are negligible [18]. The primary source of nonlinearity in gas turbine systems is the nonlinear behaviour of the unsteady heat release rate from the flames. In gas turbines, the heat release rate is influenced more strongly by the velocity perturbations than by the pressure perturbations. In general, acoustic waves can interact with entropy vorticity waves [16] and compositional waves [22]. When the unsteady perturbations are small, however, the acoustics can be approximated to behave independently of each other, except at the boundaries and zones of heat release [16]. The generation of acoustic waves due to the acceleration of entropy waves in nozzles is another mechanism of thermoacoustic oscillations [23], but is not the subject of this thesis. Most modern gas turbine systems operate with lean premixed or partially premixed flames [13]. The heat release rate of a premixed flame depends on (i) the density of the reactant flow, (ii) the burning rate or flame speed, (iii) the heat of reaction, and (iv) the flame surface area. Therefore the unsteadiness in the heat release rate depends on the fluctuations of these quantities. The fluctuations of the flame speed, in turn, depend on the perturbations in temperature, stretch rate and mixture composition of the reactant flow. The fluctuations in flame surface area depend on the disturbances that change the position and shape of the flame, which are due to fluctuations either in the flame speed or in the flow velocity. Finally, the fluctuations in the heat of reaction are due to perturbations in the mixture composition. A detailed discussion of the heat release rate response to fluctuations in each of these physical quantities is given by

Lieuwen [12].

The dynamics of premixed flames are nonlinear because of a seven-fold reason. First, the propagation of the flame normal to itself, also known as kinematic restoration, depends nonlinearly on the amplitude and wavelength of the flame wrinkle. The amplitude and wavelength of flame wrinkles, in turn, depend on the amplitude and frequency of velocity disturbances that perturb the flame [12]. Second, the flame behaviour depends not only on the instantaneous velocity field around the flame but also on the history of the velocity perturbations [26]. This is because wrinkles generated on the flame surface are advected at the velocity tangential to the flame surface and propagate along the flame until they are destroyed by flame propagation. Third, fluctuations in the velocity field can cause an oscillating flame surface to pinch off, which causes a sharp change in the flame surface area and, therefore, in the heat release rate [27]. Fourth, fluctuations in the velocity field cause local flow straining resulting in flame stretch, which affects the flame speed, and therefore the heat release rate, nonlinearly [28]. Fifth, in attached flames, the motion of the flame attachment point depends nonlinearly on the amplitude of velocity perturbations. At low velocity perturbation amplitudes, the attachment point does not move. At high perturbation velocity. amplitudes, however, the attachment point moves over a part of the cycle [29]. Furthermore, flashback may occur at high perturbation velocity amplitudes which introduces an additional nonlinearity [27]. Sixth, flame geometry affects the degree to which local nonlinear effects influence the global nonlinearities in the heat release rate (integrated over the entire flame surface) [30; 31]. In a 2-D flame the contribution of points on the flame surface close to the attachment point and further downstream to the global heat release rate are the same. In an axi-symmetric flame, however, the degree to which local nonlinear effects influence the global nonlinearities depends on the flame shape (conical, wedge-shaped etc). Seventh, fluctuations in the equivalence ratio cause fluctuations in the flame speed and heat of reaction, which are nonlinear functions of the equivalence ratio [32].

1.2   Data assimilation

Data assimilation is a mathematical and computational discipline optimally combines theory, for example in the form of a numerical model, with experimental observations. There may be a number of different goals sought, for example to determine the optimal state estimate of a system, to determine initial conditions for a numerical forecast model, to interpolate sparse observations data using (e.g. physical) knowledge of the system being observed and to train numerical model parameters based on observed data. Depending on the goal, different solution methods are used. Data assimilation is different from other forms of machine learning, image analysis, and statistical methods in that it utilizes a physical model of the system being analysed. Classically, data assimilation has been applied to chaotic dynamical systems that are too difficult to predict using simple extrapolation methods. The cause of this difficulty is that small changes in initial conditions can lead to large changes in the prediction accuracy. This is sometimes known as the butterfly effect - the sensitive dependence on initial conditions in which a small change in one state of a deterministic nonlinear system can result in large differences in a later state [47]. Numerical weather prediction models are equations describing the dynamical behavior of the atmosphere that show a chaotic behaviour. In order to use these models to make forecasts, initial conditions are needed for the model that closely resemble the current state of the atmosphere [33]. To achieve this goal, data assimilation initially developed in the field of numerical weather forecasting [34].

1.2.1   4D-Var data assimilation

The presentation of the formalism needed for properly formulating and solving variational inverse problem goes beyond the aim of this thesis. A proper introduction to the topic can be found, for instance, in [35], together with a complete description of other methods besides the variational approach (e.g. sequential methods). In the following, we provide the basics of 4D-Variational method.

Four dimensional variational data Assimilation is the process of absorbing and incorporating observed information into a model. It works under the strong constraint assumption, that
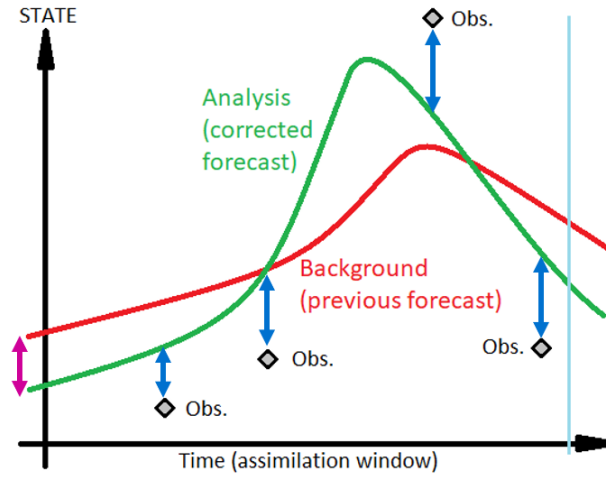
Figura 1.1 *Qualitative representation of the 4D-Var data assimilation process. The background error, J_{bg}, is proportional to the length of the pink arrow, while the observation erroor, J_{obs}, is proportional to the length of the summation of the blue arrows. The vertical cyan line stands at the end of the assimilation window, after which the forecast begins.*

is the model's equations are assumed to be perfect and the error is in the initial conditions. Therefore, we look for an estimate of the initial conditions, leaving the equations unchanged (state estimation). As will be explained in chapter 2, it possible to perform state augmentation to perform simultaneous state and parameter estimation.

Let $\mathbf{x}$ be the state vector of the model. We start from a background knowledge of the model's initial conditions, $\mathbf{x}_0^{bg}$, which we aim to improve (i.e. to be as close as possible to the true, unknown, initial conditions). Integrating the system from $\mathbf{x}_0^{bg}$, we obtain the red trajectory in figure (1.1), $\mathbf{x}^{bg}(t)$. We assume to have a set of observations, which are distributed over an assimilation window at some time instants. We define a cost functional (J_{obs}) that measures the distance between the background trajectory and the observations. We compute the gradient of the cost functional with respect to the initial conditions ($\nabla_{\mathbf{x}_0}(J)$) with the aid of adjoint equations. Then, we update $\mathbf{x}_0^{bg} = \mathbf{x}_0^{(1)}$ using a gradient based approach (e.g. steepest descent), obtaining $\mathbf{x}_0^{(2)}$. We repeat this process N times, until we meet the condition $\nabla_{\mathbf{x}_0}(J) = 0$, which correspond to the a minimum of the cost functional, and we call $\mathbf{x}_0^N = \mathbf{x}_0^{analysis}$. The analysis trajectory corresponds to the green line in figure (1.1) and it is obtained by integrating the same model, which produces the background and the true solution (strong constraint approximation). In order to weigh also the background knowledge,

we include in the cost functional a term that measures the distance between the current initial condition and the background initial condition, J_{bg} (pink arrow in figure 1.1). If we had considered J_{obs} only, we would have used the background knowledge as a first guess for the initial conditions but the optimal solution would not have been affected by $\mathbf{x}_0^{bg}$.

Both observations and $\mathbf{x}_0^{bg}$ are assumed to have unbiased error. We also assume that we know the statistical behaviour of the error terms, through their first and second order moments. We call $\mathbf{B}$ and $\mathbf{R}$ the covariance matrices describing the statistical behaviour of the background and observations errors, respectively. In practice, the cost functional we minimise is defined as

$$
\begin{aligned}
J &= J_{bg} + J_{obs} \\
&= \frac{1}{2}||\mathbf{x}_0 - \mathbf{x}_0^{bg}||_{\mathbf{B}}^2 + \frac{1}{2}\sum_{i=1}^{N_{obs}}||\mathbf{x}(t_{obs}^i) - \mathbf{y}^i||_{\mathbf{R}}^2,
\end{aligned}
\tag{1.1}
$$

where "bg" stands for "background", "$\mathbf{y}^i$" is the i-th observed state vector (or a linear function of the state vector at the time of the i-th measurement, t_{obs}^i) and N_{obs} is the number of observations. The notation $||\cdot||_B^2$ is the squared norm based on the matrix $\mathbf{B}$, which reads

$$
||\mathbf{x}_0 - \mathbf{x}_0^{bg}||_{\mathbf{B}}^2 = \left(\mathbf{x}_0 - \mathbf{x}_0^{bg}\right)^{\mathrm{T}} \mathbf{B}^{-1} \left(\mathbf{x}_0 - \mathbf{x}_0^{bg}\right) .
\tag{1.2}
$$

The vector norms based on the covariance matrices are called statistical distances. In our work we assume that $\mathbf{R}$ and $\mathbf{B}$ are diagonal, and that the nonzero elements are all equal to $\sigma_{obs}^2 = R$ and $\sigma_{bg}^2 = B$ respectively. $\mathbf{R}$ and $\mathbf{B}$ being diagonal means that we assume statistically independent errors.

The outcome of the assimilation process is the analysis solution, which is optimal as it corresponds to the minimum of (i) the statistical distance between itself and the observations and (ii) between its initial conditions and the background initial conditions.

1.3 Scope and structure of the thesis

Performing state and parameter estimation is one of the central problem in thermoacoustics. The first aim of the thesis is to apply the framework of 4-dimensional variational data assimilation for state estimation to a low-order thermoacoustic model. We chose to work with an $n - \tau$ nonlinear model of a horizontal Rijke tube [36] which can capture the essential physics underlying thermoacoustic instabilities. Along with state augmentation and parameter estimation, this method can be applied for real-time calibration of thermoacoustic models and to predict in a quantitative manner thermoacoustic oscillations.

1.3.1 Structure of the thesis

Chapter 2 introduces the thermoacoustic model of a Rijke tube. The governing equations are decomposed in natural acoustic modes (Galerkin modes) and the dynamical system describing their amplitudes is presented. We perform state augmentation of such a dynamical system, including the thermoacoustic parameters into the state vector. The adjoint equations of the augmented state are derived. The last section describes the tests that are used to check the adjoint codes.

In chapter 3 results of 4D-Var data assimilation twin experiments on the thermoacoustic model are performed and commented. First, it is shown how the number of computed acoustic modes affects the solution of the system and how the twin experiments are set up. Then, we describe the details of the cost functional specific to the thermoacoustic application of data assimilation. We compute the first 10 natural acoustic modes of the Rijke tube to capture the transient dynamics, and we observe that the outcome of the assimilation strongly depends on whether (or not) we assimilate data in the transient or at regime. A new, more effective, cost functional for the observations error is proposed to assimilate data during transient dynamics. Three different cost functional for the observation error are commented. Finally, we show the effects on the analysis trajectory of the number of observations, their time distribution over the assimilation window and the frequency of observation.

Chapter 4 examines the computational cost of data assimilation. The analysis is carried out with two different types of cost functional in the chaotic Lorenz system. It is shown how the gradient computation depends on the choice between the continuous (CA) and the discrete adjoint (DA) approach. Then, referring to the thermoacoustic model, the computational cost of data assimilation using sensitivity analysis is estimated. It is compared with the computational cost using the CA method. Finally, we present and discuss the conclusions of this work and future directions.

Capitolo 2

The thermoacoustic model and its adjoint

Introduction

Chapter 3 provides the mathematical background necessary to perform 4D-Var data assimilation on the thermoacoustic model of a horizontal Rijke tube. The thermoacoustic model of a horizontal Rijke tube is introduced and adimensionalised. Then, the solution is decomposed using a basis of orthogonal functions, sometimes referred to as Galerkin modes.

The augmented system is presented, which includes the model's parameters into the state vector with a view to parameter estimation. In principle, the adjoint of the governing equations should be derived first, as they are used for state estimation. However, we choose to derive the adjoint of the augmented system first. It stems from the fact that such a derivation contains the one for the adjoint governing equations alone, allowing us not to repeat the latter.

For both the original and the augmented system the continuous approach in used to derive the adjoint equations. Such equations are solved numerically with a Runge-Kutta $4-th$ order scheme and tested (gradient test and dot-product test). These tests are described in section 2.3.

2.1   The thermoacoustic model

2.1.1   The dimensional governing equations and their boundary conditions

The thermoacoustic system examined in this work is a horizontal Rijke tube of length L_0 in which a hot wire is placed at a distance $\tilde{x}_f$ from one end. A base flow is imposed through the tube with velocity u_0. The physical properties of the gas in the tube are described by c_v, γ, R and λ, which represent the constant volume specific heat capacity, the ratio of specific heats, the gas constant and the thermal conductivity, respectively. The unperturbed quantities of the base flow are ρ_0, p_0 and T_0, which represent density, pressure and temperature, respectively. From these, one can derive the speed of sound $c_0 \equiv \sqrt{\gamma R T_0}$ and the Mach number of the flow $M \equiv u_0/c_0$.

Acoustic perturbations are considered on top of this base flow. In dimensional form, the perturbation velocity and perturbation pressure are represented by the variables $\tilde{u}$ and $\tilde{p}$, respectively, and distance and time are represented by the coordinates $\tilde{x}$ and $\tilde{t}$, respectively. Quantities evaluated at the hot wire's position, $\tilde{x}_f$, have the subscript f. At the hot wire, the rate of heat transfer to the gas is given by $\tilde{Q}$. This heat transfer is applied at the wire's position by multiplying $\tilde{Q}$ by the dimensional Dirac delta distribution $\tilde{\delta}_D(\tilde{x} - \tilde{x}_f)$. Acoustic damping is represented by ζ.

The dimensional governing equations for the perturbation are the momentum equation and the energy equation [36]:

$$\tilde{F}_1 \equiv \rho_0 \frac{\partial \tilde{u}}{\partial \tilde{t}} + \frac{\partial \tilde{p}}{\partial \tilde{x}} = 0 \tag{2.1}$$

$$\tilde{F}_2 \equiv \frac{\partial \tilde{p}}{\partial \tilde{t}} + \gamma p_0 \frac{\partial \tilde{u}}{\partial \tilde{x}} + \zeta \frac{c_0}{L_0} \tilde{p} - (\gamma - 1)\tilde{Q}\tilde{\delta}_D(\tilde{x} - \tilde{x}_f) = 0 \tag{2.2}$$

They are derived under the assumption of uniform mean flow with zero Mach number. It is also assumed longitudinal acoustics, that is the length of the tube is much larger than its diameter, resulting in a high cut-on frequency. The heat release term is modelled with a form of King's law adapted by [38,39]. Here the terms that express the effect of the velocity are

modified, employing a 5th order polynomial, $\text{Poly}(\tilde{u}(\tilde{t})) = a_1\tilde{u}^5(\tilde{t}) + \cdots + a_5\tilde{u}(\tilde{t})$. Surface heat transfer and subsequent thermal diffusion between the wire and the fluid are modelled by a constant time delay, $\tilde{\tau}$, between the time when the velocity acts and the time when the corresponding heat release is felt by the perturbation

$$\tilde{\dot{Q}} = \frac{2L_w(T_w - T_0)}{s}\left(\pi\lambda c_v\rho_0\frac{d_w}{2}\right)^{1/2}\text{Poly}(\tilde{u}_f(\tilde{t} - \tilde{\tau})) , \qquad (2.3)$$

where L_w, d_w and T_w represent the length, diameter and temperature of the wire, respectively, and S represents the cross-sectional area of the tube. This model contains a time delay and a simple model for nonlinear attenuation, which are the two most influential features in more sophisticated flame models [40,41,42]. Ideal boundary conditions are employed

$$\partial u/\partial x = 0 \qquad \tilde{x} = 0, L_0 \qquad\qquad (2.4)$$

$$p = 0 \qquad \tilde{x} = 0, L_0. \qquad\qquad (2.5)$$

The energy radiation by the boundary is modelled by the damping coefficient in the energy equation (2.2).

2.1.2   The non-dimensional governing equations

Reference scales for speed, pressure, length and time are taken to be $U_0, p_0\gamma M, L_0$ and L_0/c_0, respectively. The dimensional variables, coordinates and Dirac delta can then be written as

$$\tilde{u} = u_0 u, \;\; \tilde{p} = p_0\gamma M p, \;\; \tilde{x} = L_0 x, \;\; \tilde{t} = \frac{L_0}{c_0}t, \;\; \tilde{\delta}_D(\tilde{x} - \tilde{x}_f) = \frac{\delta_d(x - x_f)}{L_0}, \qquad (2.6)$$

where the quantities without a tilde or subscript 0 are dimensionless.

Substituting (2.6) into the dimensional governing equations (2.1) and (2.2) and making use of the definition of c_0 and the ideal gas law, $p_0 = \rho_0 R T_0$, gives the dimensionless

governing equations

$$F_1 \equiv \frac{\partial u}{\partial t} + \frac{\partial p}{\partial x} = 0, \tag{2.7}$$

$$F_2 \equiv \frac{\partial p}{\partial t} + \frac{\partial u}{\partial x} + \zeta p - \beta \text{Poly}(u_f(t-\tau))\delta_D(x-x_f) = 0, \tag{2.8}$$

where

$$\beta \equiv \frac{1}{p_0\sqrt{u_0}} \frac{2L_w(T_w - T_0)}{S} \left(\pi \lambda c_v \rho_0 \frac{d_w}{2} \right)^{1/2}. \tag{2.9}$$

The system has four control parameters: ζ, which is the damping; β, which encapsulates all relevant information about the hot wire, base velocity and ambient conditions; τ, which is the time delay; and x_f, which is the position of the wire. The latter be fixed, hence not included in the augmented state for parameter estimation.

2.1.3   The discretised governing equations

With appropriate boundary and initial conditions, the governing equations (2.7) and (2.8) are a system of partial differential equations. The boundary conditions (2.4) and (2.5) are enforced by choosing the basis of the natural acoustic modes, which read

$$u(x,t) = \sum_{j=1}^{N_m} \eta_j(t)\cos(j\pi x), \tag{2.10}$$

$$p(x,t) = \sum_{j=1}^{N_m} \left(\frac{\dot{\eta}_j(t)}{j\pi} \right) \sin(j\pi x), \tag{2.11}$$

where the relationship between η_j and $\dot{\eta}_j$ has not yet been specified. In this discretization, which is sometimes known as the Galerkin discretization, all the basis vectors are orthogonal.

The state of the system is given by the amplitudes of the Galerkin modes that represent velocity, η_j, and those that represent pressure, $\frac{\dot{\eta}_j}{j\pi}$. In vector notation $\mathbf{u} \equiv (\eta_1, \cdots, \eta_N)^{\text{T}}$ and $\mathbf{p} \equiv (\frac{\dot{\eta}_1}{\pi}, \cdots, \frac{\dot{\eta}_N}{N\pi})^{\text{T}}$. The state vector of the discretized system is the column vector $\mathbf{x} \equiv (\mathbf{u};\mathbf{p})$, with N_m degrees of freedom.

The governing equations are discretized by substituting (2.10) and (2.11) into (2.7) and (2.8). The damping, ζ, is dealt with by assigning a damping parameter, ζ_j, to each mode [43]. Equation (2.8) is then multiplied by $\sin(k\pi x)$ and integrated over the domain $x = [0, 1]$. The governing equations then can be reduced to a system of delay differential equations (DDEs) for each mode, j:

$$F_{1j} \equiv \frac{d}{dt}\left(\eta_j\right) - j\pi\left(\frac{\dot{\eta}_j}{j\pi}\right) = 0, \tag{2.12}$$

$$F_{2j} \equiv \frac{d}{dt}\left(\frac{\dot{\eta}_j}{j\pi}\right) + j\pi\eta_j + \zeta_j\left(\frac{\dot{\eta}_j}{j\pi}\right) = 0 \quad \text{for } t \in [0, \tau), \tag{2.13}$$

$$F_{2j} \equiv \frac{d}{dt}\left(\frac{\dot{\eta}_j}{j\pi}\right) + j\pi\eta_j + \zeta_j\left(\frac{\dot{\eta}_j}{j\pi}\right) + 2s_j\,\beta\,\mathrm{Poly}(u_f(t-\tau)) = 0 \quad \text{for } t \in [\tau, T], \tag{2.14}$$

where

$$u_f(t-\tau) = \sum_{j=1}^{N_m} \eta_j(t-\tau)c_j, \tag{2.15}$$

$s_j \equiv \sin(j\pi x_f)$ and $c_j \equiv \cos(j\pi x_f)$. Equations F_{2j}, for $j = 1, \cdots, N_{mod}$, are piecewise because when numerical integration is performed the value of $u_f(t-\tau)$ is not available for $t < \tau$. When parameter estimation is performed many sets of parameters are compared. We recommend to introduce a new parameter $t^* > \tau$, which does not need to be optimised, corresponding to the time interval over which equation (2.13) holds. It allows us to compare different sets of parameters keeping the time interval over which $\dot{Q} \neq 0$ unchanged and equal to $[t^*, T]$.

2.2 The augmented-state system and its adjoint

In this section the equations for constrained optimisation of the nonlinear augmented-state system are derived (adjoint equations) with cost functional

$$J = \sum_{j=1}^{N_{mod}} J_j \quad \text{where} \quad J_j = \eta_j^2(T) + \left(\frac{\dot{\eta}_j(T)}{j\pi}\right)^2. \tag{2.16}$$

As explained in chapter 4, section 4.1, we can encounter two physically significant types of cost functionals. This is analogous to the one reported in equation (4.2) and it represents the acoustic energy at $t = T$. For the purpose of this section, using such a definition has at least three advantages: First, it does not add any forcing term in the adjoint equations. Second, it is equivalent to the cost functionals utilised in data assimilation. Third, its derivatives are easy to compute, so unnecessary complications are avoided. The derivatives of J actually employed in the twin experiments discussed in this work are reported in chapter 3, sections (3.3.1) and (3.3.2).

2.2.1   Definition of the Lagrangian

Let $\mathbf{p}$ be the vector of thermoacoustic parametres $[\beta, \ \tau, \ \zeta_1, \ \dots, \zeta_{N_{mod}}]^{\mathrm{T}}$ and $\hat{\mathbf{x}}$ be the state vector of the *augmented system*. The augmented-state system can be written as

$$\frac{d}{dt}\hat{\mathbf{x}} = \frac{d}{dt}\begin{bmatrix} \mathbf{x} \\ \mathbf{p} \end{bmatrix} = \begin{bmatrix} F(\mathbf{x},\mathbf{p}) \\ \mathbf{0} \end{bmatrix} = \hat{F}(\hat{\mathbf{x}}), \tag{2.17}$$

with initial conditions

$$\hat{\mathbf{x}}(t_0) = \begin{bmatrix} \mathbf{x}_0 \\ \mathbf{p}_0 \end{bmatrix} = \hat{\mathbf{x}}_0 \ . \tag{2.18}$$

The governing equation and their initial conditions are written in the form of constraints, F, which hold over time intervals while G are the ones that hold for a specific time only, i.e.

$t = t_0$. They read

$$F_{1j} \equiv \frac{d}{dt}\left(\eta_j\right) - j\pi\left(\frac{\dot{\eta}_j}{j\pi}\right) = 0, \tag{2.19}$$

$$F_{2j} \equiv \frac{d}{dt}\left(\frac{\dot{\eta}_j}{j\pi}\right) + j\pi\eta_j + \zeta_j\left(\frac{\dot{\eta}_j}{j\pi}\right) = 0 \qquad \text{for } t \in [0,t^*), \tag{2.20}$$

$$F_{2j} \equiv \frac{d}{dt}\left(\frac{\dot{\eta}_j}{j\pi}\right) + j\pi\eta_j + \zeta_j\left(\frac{\dot{\eta}_j}{j\pi}\right) + 2s_j\beta\,\mathrm{Poly}(\bar{\eta}(t)) = 0 \qquad \text{for } t \in [t^*,T], \tag{2.21}$$

$$F_3 \equiv \bar{\eta}(t) = 0, \qquad \text{for } t \in [0,t^*) \tag{2.22}$$

$$F_3 \equiv \bar{\eta}(t) - u_f(t-\tau) = 0, \qquad \text{for } t \in [t^*,T] \tag{2.23}$$

$$F_4 \equiv \frac{d\beta}{dt} = 0, \tag{2.24}$$

$$F_5 \equiv \frac{d\tau}{dt} = 0, \tag{2.25}$$

$$F_{6j} \equiv \frac{d\zeta_j}{dt} = 0, \tag{2.26}$$

where $\mathrm{Poly}(\bar{\eta}(t)) = a_1\bar{\eta}^5 + \cdots + a_5\bar{\eta}$ is the heat release term and $u_f(t-\tau)$ is the velocity at the flame position, defined in equation (2.15). The contraints for the initial conditions are

$$G_{1j} \equiv \eta_j(0) - \eta_{j0} = 0, \tag{2.27}$$

$$G_{2j} \equiv \left(\frac{\dot{\eta}_j(0)}{j\pi}\right) - \left(\frac{\dot{\eta}_{j0}}{j\pi}\right) = 0, \tag{2.28}$$

$$G_4 \equiv \beta(0) - \beta_0 = 0, \tag{2.29}$$

$$G_5 \equiv \tau(0) - \tau_0 = 0, \tag{2.30}$$

$$G_{6j} \equiv \zeta_j(0) - \zeta_{j0} = 0. \tag{2.31}$$

By defining the inner product as

$$[a(t), b(t)] = \frac{1}{T}\int_0^T ab\, dt, \tag{2.32}$$

the Lagrangian can be written as

$$\mathscr{L} \equiv \sum_{j=1}^{N_{mod}} \mathscr{L}_j - \left[\bar{\bar{\xi}}(t), F_3\right] - \left[\beta^+, F_4\right] - \left[\tau^+, F_5\right] - b_4 G_4 - b_5 G_5, \qquad (2.33)$$

where each $\mathscr{L}_j$ is

$$\mathscr{L}_j \equiv J_j - \left[\frac{\xi_j}{j\pi}, F_{1j}\right] - \left[v_j, F_{2j}\right] - \left[\zeta_j^+, F_{6j}\right] - b_{1j} G_{1j} - b_{2j} G_{2j} - b_{6j} G_{6j} . \qquad (2.34)$$

In equation (2.33) and (2.34) $\bar{\bar{\xi}}$, β^+, τ^+ and $\xi_j/j\pi$, v_j, ζ_j^+ for $j = 1, \cdots, N_{mod}$ are introduced. They are the Lagrange multipliers or adjoint variables.

The time delay term in eq. (2.33) is manipulated through a change of variables, allowing us to transfer the shifting in time from the direct to the adjoint variable. This is useful when the conditions to find an extremum of $\mathscr{L}$ are imposed to derive the adjoint equations, as will be explained in section 2.2.3. By performing the change of variable, we start from

$$
\begin{aligned}
\left[\bar{\bar{\xi}}(t), F_3\right] &= \left[\bar{\bar{\xi}}(t), \bar{\eta}(t)\right] - \left[\bar{\bar{\xi}}(t), u_f(t-\tau)\right] \\
&= \left[\bar{\bar{\xi}}(t), \bar{\eta}(t)\right]_0^{t^*} + \left[\bar{\bar{\xi}}(t), \bar{\eta}(t)\right]_{t^*}^{T} - \left[\bar{\bar{\xi}}(t), u_f(t-\tau)\right]_{t^*}^{T},
\end{aligned} \qquad (2.35)
$$

where the first term on the RHS is zero. This holds because $u_f(t)$ is assumed to be zero for $t < 0$. Then, we set $t' = t - \tau$ to obtain

$$
\begin{aligned}
\left[\bar{\bar{\xi}}(t), u_f(t-\tau)\right]_{t^*}^{T} &= \frac{1}{T} \int_{t^*}^{T} \bar{\bar{\xi}}(t) u_f(t-\tau) dt \\
&= \frac{1}{T} \int_{t^*-\tau}^{T-\tau} \bar{\bar{\xi}}(t'+\tau) u_f(t') dt' \\
&= \left[\bar{\bar{\xi}}(t'+\tau), u_f(t')\right]_{t^*-\tau}^{T-\tau}
\end{aligned} \qquad (2.36)
$$

In the RHS of equation (2.36) there is an inner product that, as such, does not depend on the integration variable t', therefore t' can be replaced with t, giving

$$\left[\bar{\xi}(t), u_f(t-\tau)\right]_{t*}^{T} = \left[\bar{\xi}(t+\tau), u_f(t)\right]_{t*-\tau}^{T-\tau}. \tag{2.37}$$

Finally, from equation (2.35) we obtain

$$\left[\bar{\xi}(t), \mathrm{F}_3\right] = \left[\bar{\xi}(t), \bar{\eta}(t)\right]_{t*}^{T} - \left[\bar{\xi}(t+\tau), u_f(t)\right]_{t*-\tau}^{T-\tau}. \tag{2.38}$$

Now, each inner product terms in the Lagrangian, (2.33), which has a time derivative, is rearranged to show an explicit dependence on the direct variables. To do so each of them is integrated by parts, yelding

$$
\begin{aligned}
\mathscr{L} = &\sum_{j=1}^{N_{mod}} J_j \\
&- \sum_{j=1}^{N_{mod}} \left\{ -\left[\frac{d}{dt}\left(\frac{\xi_j}{j\pi}\right), \eta_j\right] - \left[j\pi\frac{\xi_j}{j\pi}, \frac{\dot{\eta}_j}{j\pi}\right] + \frac{1}{T}\left(\frac{\xi_j(T)}{j\pi}\eta_j(T) - \frac{\xi_j(0)}{j\pi}\eta_j(0)\right) \right\} \\
&- \sum_{j=1}^{N_{mod}} \left\{ -\left[\frac{dv_j}{dt}, \frac{\dot{\eta}_j}{j\pi}\right] + \left[j\pi v_j, \eta_j\right] + \left[\zeta_j v_j, \frac{\dot{\eta}_j}{j\pi}\right] + \Re_j + \frac{1}{T}\left(v_j(T)\frac{\dot{\eta}_j(T)}{j\pi} - v_j(0)\frac{\dot{\eta}_j(0)}{j\pi}\right) \right\} \\
&- \sum_{j=1}^{N_{mod}} \left\{ b_{1j}\left(\eta_j(0) - \eta_{j0}\right) + b_{2j}\left(\frac{\dot{\eta}_j(0)}{j\pi} - \frac{\dot{\eta}_{j0}}{j\pi}\right) \right\} \\
&- \sum_{j=1}^{N_{mod}} \left\{ b_{6j}\left(\zeta_j(0) - \zeta_{j0}\right) - \left[\frac{d\zeta_j^+}{dt}, \zeta_j\right] + \frac{1}{T}\left(\zeta_j^+(T)\zeta_j(T) - \zeta_j^+(0)\zeta_j(0)\right) \right\} \\
&- \left\{ \left[\bar{\xi}(t), \bar{\eta}(t)\right] - \left[\bar{\xi}(t+\tau), u_f(t)\right]_{t*-\tau}^{T-\tau} \right\} \\
&- \left\{ \frac{1}{T}\left(\beta^+(T)\beta(T) - \beta^+(0)\beta(0)\right) - \left[\frac{d\beta^+}{dt}, \beta\right] \right\} - b_4\left(\beta(0) - \beta_0\right) \\
&- \left\{ \frac{1}{T}\left(\tau^+(T)\tau(T) - \tau^+(0)\tau(0)\right) - \left[\frac{d\tau^+}{dt}, \tau\right] \right\} - b_5\left(\tau(0) - \tau_0\right),
\end{aligned}
\tag{2.39}
$$

where

$$\mathfrak{R}_j = \left[\ v_j, 2\beta\ s_j\ \text{Poly}(\bar{\eta}(t))\ \right]\ . \tag{2.40}$$

2.2.2 Linearisation

The next step is to linearise the Lagrangian. When linearisations are performed with respect to functions, the Frechet derivative[1] is used

$$\left[\frac{\partial \mathscr{L}}{\partial x}, \delta x\right] \equiv \lim_{\varepsilon \to 0} \frac{\mathscr{L}(x + \varepsilon \delta x) - \mathscr{L}(x)}{\varepsilon}\ . \tag{2.41}$$

We find

$$\left[\frac{\partial \mathscr{L}}{\partial \eta_j}, \delta \eta_j\right] = \left[\frac{d}{dt}\left(\frac{\xi_j}{j\pi}\right) - j\pi v_j, \delta \eta_j\right] - \frac{1}{T}\frac{\xi_j(T)}{j\pi}\delta \eta_j(T) + \left(\frac{1}{T}\frac{\xi_j(0)}{j\pi} - b_{1j}\right)\delta \eta_j(0)$$
$$+ 2\eta_j(T)\delta \eta_j(T) + \left[\bar{\xi}(t+\tau)c_j, \delta \eta_j(t)\right]_{t^*-\tau}^{T-\tau}, \tag{2.42}$$

$$\left[\frac{\partial \mathscr{L}}{\partial \left(\frac{\dot{\eta}_j}{j\pi}\right)}, \delta\left(\frac{\dot{\eta}_j}{j\pi}\right)\right] = \left[\frac{dv_j}{dt} + j\pi\frac{\xi_j}{j\pi} + \zeta_j v_j, \delta\left(\frac{\dot{\eta}_j}{j\pi}\right)\right] - \frac{1}{T}v_j(T)\delta\left(\frac{\dot{\eta}_j(T)}{j\pi}\right)$$
$$+ \left(\frac{1}{T}v_j(0) - b_{2j}\right)\delta\left(\frac{\dot{\eta}_j(0)}{j\pi}\right) + 2\frac{\dot{\eta}_j(T)}{j\pi}\delta\left(\frac{\dot{\eta}_j(T)}{j\pi}\right), \tag{2.43}$$

Note that the summations over j disappear in eqs. (2.42) and (2.43) because the derivatives are taken with respect to the j-th mode. All η_k with $k \neq j$ do not give any contribution. The terms in cyan above and in the following equations are the ones that may change depending on which cost functional we use.

$$\left[\frac{\partial \mathscr{L}}{\partial \bar{\eta}(t)}, \delta\bar{\eta}(t)\right] = -\left[\sum_{j=1}^{N_{mod}}\left(5a_1\bar{\eta}^4 + 4a_2\bar{\eta}^3 + 3a_3\bar{\eta}^2 + 2a_4\bar{\eta} + a_5\right)2v_j s_j\beta, \delta\bar{\eta}(t)\right] - \left[\bar{\xi}, \delta\bar{\eta}\right], \tag{2.44}$$

---

[1]Named after Maurice Frechet, it is commonly used to generalize the derivative of a real-valued function of a single real variable to the case of a real vector-valued function, and to define the functional derivative, widely used in the calculus of variations.

Note that in equation (2.44) the summation does not disappear because the derivative is taken with respect to a global variable, that is without the j subscript.

The equations below are the derivatives with respect to the parametres. Using the method of the *augmented state* they are regarded as state variables of the system, so the derivation is carried out in the same way as above, giving

$$
\left[\frac{\partial \mathscr{L}}{\partial \beta}, \delta\beta\right] = -\left[\sum_{j=1}^{N_{mod}} 2v_j s_j \operatorname{Poly}(\bar{\eta}), \delta\beta(t)\right] + \left[\frac{d\beta^+}{dt}, \delta\beta\right] - \frac{1}{T}\beta^+(T)\delta\beta(T)
$$
$$
+ \left(\frac{1}{T}\beta^+(0) - b_4\right)\delta\beta(0), \tag{2.45}
$$

$$
\left[\frac{\partial \mathscr{L}}{\partial \zeta_j}, \delta\zeta_j\right] = \left[\frac{d\zeta_j^+}{dt}, \delta\zeta_j\right] - \left[v_j \frac{\dot{\eta}_j}{j\pi}, \delta\zeta_j\right] - \frac{1}{T}\zeta_j^+(T)\delta\zeta_j(T) + \left(\frac{1}{T}\zeta_j^+(0) - b_{6j}\right)\delta\zeta_j(0).
$$
$$
\tag{2.46}
$$

The parameter τ appears also in the term $\left[\bar{\xi}(t+\tau), u_f(t)\right]_{t^*-\tau}^{T-\tau}$ of eq. (2.39), because τ is in both the limits of integration and the integral's argument. To compute this derivative, equation (2.41) is used, to yield

$$
\lim_{\varepsilon\to 0} \frac{1}{\varepsilon T}\left\{\int_{t^*-\tau-\varepsilon\delta\tau}^{T-\tau-\varepsilon\delta\tau} \bar{\xi}(t+\tau+\varepsilon\delta\tau)u_f(t)dt - \int_{t^*-\tau}^{T-\tau} \bar{\xi}(t+\tau)u_f(t)dt\right\}. \tag{2.47}
$$

The second integral inside the curly brackets can be written as

$$
\int_{t^*-\tau-\varepsilon\delta\tau}^{T-\tau-\varepsilon\delta\tau} \bar{\xi}(t+\tau+\varepsilon\delta\tau)u_f(t+\varepsilon\delta\tau)dt.
$$

The integrals in equation (2.47) share the limits of integration, yielding

$$\lim_{\varepsilon \to 0} -\frac{1}{T} \int\limits_{t^*-\tau-\varepsilon\delta\tau}^{T-\tau-\varepsilon\delta\tau} \bar{\xi}(t+\tau+\varepsilon\delta\tau)\frac{u_f(t+\varepsilon\delta\tau)-u_f(t)}{\varepsilon\delta\tau(t)}\delta\tau(t)dt =$$

$$= -\frac{1}{T} \int\limits_{t^*-\tau}^{T-\tau} \bar{\xi}(t+\tau)\frac{du_f(t)}{dt}\delta\tau(t)dt \ . \tag{2.48}$$

Finally, the derivative of $\mathscr{L}$ with respect to τ reads

$$\left[\frac{\partial \mathscr{L}}{\partial \tau}, \delta\tau\right] = -\left[\bar{\xi}(t-\tau)\frac{du_f(t)}{dt}, \delta\tau(t)\right]_{t^*-\tau}^{T-\tau}$$

$$+ \left[\frac{d\tau^+}{dt}, \delta\tau\right] - \frac{1}{T}\tau^+(T)\delta\tau(T) + \left(\frac{1}{T}\tau^+(0) - b_5\right)\delta\tau(0). \tag{2.49}$$

The next step is to take the derivatives of $\mathscr{L}$ with respect to the initial condition of every direct variable of the augmented state to provide the gradient information. The derivatives read

$$\left[\frac{\partial \mathscr{L}}{\partial \eta_{j0}}, \delta\eta_{j0}\right] = 0 + b_{1j}\delta\eta_{j0}, \tag{2.50}$$

$$\left[\frac{\partial \mathscr{L}}{\partial \beta_0}, \delta\beta_0\right] = b_4 \ \delta\beta_0, \tag{2.51}$$

$$\left[\frac{\partial \mathscr{L}}{\partial \frac{\dot{\eta}_{j0}}{j\pi}}, \delta\left(\frac{\dot{\eta}_{j0}}{j\pi}\right)\right] = 0 + b_{2j}\left(\frac{\dot{\eta}_{j0}}{j\pi}\right), \tag{2.52}$$

$$\left[\frac{\partial \mathscr{L}}{\partial \zeta_{j0}}, \delta\zeta_{j0}\right] = b_{6j} \ \delta\zeta_{j0}, \tag{2.53}$$

$$\left[\frac{\partial \mathscr{L}}{\partial \tau_0}, \delta\tau_0\right] = b_5 \ \delta\tau_0. \tag{2.54}$$

2.2.3 Adjoint Equations

To find the set of functions that characterises an extremum for the functional $\mathscr{L}$, variations with respect to $\delta\hat{\mathbf{x}}$ are set to zero in equations (2.42) to (2.46) and (2.49). By proceeding

sequentially, variations in η_j are set to zero in $[0,T]$, yelding

$$\frac{d}{dt}\left(\frac{\xi_j}{j\pi}\right) - j\pi v_j + \bar{\xi}(t+\tau)c_j = 0 \qquad t \in [t^* - \tau, T - \tau], \tag{2.55}$$

$$\frac{d}{dt}\left(\frac{\xi_j}{j\pi}\right) - j\pi v_j = 0 \qquad t \in [0, t^* - \tau) \cup (T - \tau, T], \tag{2.56}$$

$$2\eta_j(T) - \frac{1}{T}\left(\frac{\xi_j(T)}{j\pi}\right) = 0 \qquad t = T, \tag{2.57}$$

$$\frac{1}{T}\left(\frac{\xi_j(0)}{j\pi}\right) - b_{1j} = 0 \qquad t = 0. \tag{2.58}$$

Variations in $\left(\frac{\dot{\eta}_j}{j\pi}\right)$ are set to zero in $[0,T]$, yelding

$$\frac{d}{dt}v_j + j\pi\left(\frac{\xi_j}{j\pi}\right) + \zeta_j v_j = 0 \qquad t \in [0,T], \tag{2.59}$$

$$2\left(\frac{\dot{\eta}_j(T)}{j\pi}\right) - \frac{1}{T}v_j(T) = 0 \qquad t = T, \tag{2.60}$$

$$\frac{1}{T}v_j(0) - b_{2j} = 0 \qquad t = 0. \tag{2.61}$$

Variations in $\bar{\eta}$ are set to zero in $[0,T]$, yelding

$$-\bar{\xi}(t) - \sum_{j=1}^{N_{mod}} 2v_j s_j \left(5a_1\bar{\eta}^4 + 4a_2\bar{\eta}^3 + 3a_3\bar{\eta}^2 + 2a_4\bar{\eta} + a_5\right)\beta = 0 \qquad t \in [0,T]. \tag{2.62}$$

Variations in β are set to zero in $[0,T]$, yelding

$$\frac{d}{dt}\beta^+ - \sum_{j=1}^{N_{mod}} 2v_j s_j \mathrm{Poly}(\bar{\eta}(t)) = 0 \qquad t \in [0,T], \tag{2.63}$$

$$\frac{1}{T}\beta^+(T) = 0 \qquad t = T, \tag{2.64}$$

$$\frac{1}{T}\beta^+(0) - b_4 = 0 \qquad t = 0. \tag{2.65}$$

Variations in ζ_j are set to zero in $[0,T]$, yelding

$$\frac{d}{dt}\zeta_j^+ - v_j\left(\frac{\dot{\eta}_j}{j\pi}\right) = 0 \qquad t \in [0,T], \qquad (2.66)$$

$$-\frac{1}{T}\zeta_j^+(T) = 0 \qquad t = T, \qquad (2.67)$$

$$\frac{1}{T}\zeta_j^+(0) - b_{6j} = 0 \qquad t = 0. \qquad (2.68)$$

Finally, variations in τ are set to zero in $[0,T]$. From equation (2.49) it follows

$$\frac{d}{dt}\tau^+ - \bar{\xi}(t+\tau)\frac{du_f(t)}{dt} = 0 \qquad t \in [t^* - \tau, T - \tau], \qquad (2.69)$$

$$\frac{d}{dt}\tau^+ = 0 \qquad t \in [0, t^* - \tau) \cup (T - \tau, T], \qquad (2.70)$$

$$\tau^+(t) = 0 \qquad t = T, \qquad (2.71)$$

$$\frac{1}{T}\tau^+(0) - b_5 = 0 \qquad t = 0. \qquad (2.72)$$

2.2.4 Gradient-based optimisation

The optimisation loop consists of the following steps:

1) Start from an initial state $\hat{\mathbf{x}}_0$ (in twin experiments it is the background initial condition);

2) Integrate the system forward to $t = T$;

3) Initialise the adjoint variables using equations (2.57), (2.60), (2.64), (2.67) and (2.71);

4) Evolve the adjoint variable backwards from $t = T$ to $t = 0$;

5) Evaluate the gradient using equations (2.58), (2.61), (2.65), (2.68) and (2.72) together with equations (2.50) to (2.54).

Once the gradient is numerically computed, the cost functional can be minimised via a gradient based optimization loop. Several different optimisation routines can be used to update the gradient up to $\nabla_{\hat{\mathbf{x}}_0}(J) = 0$, such as the steepest descent or conjugate gradient [44]. The latter was implemented in the majority of the cases shown in this work because

(a)   (b)
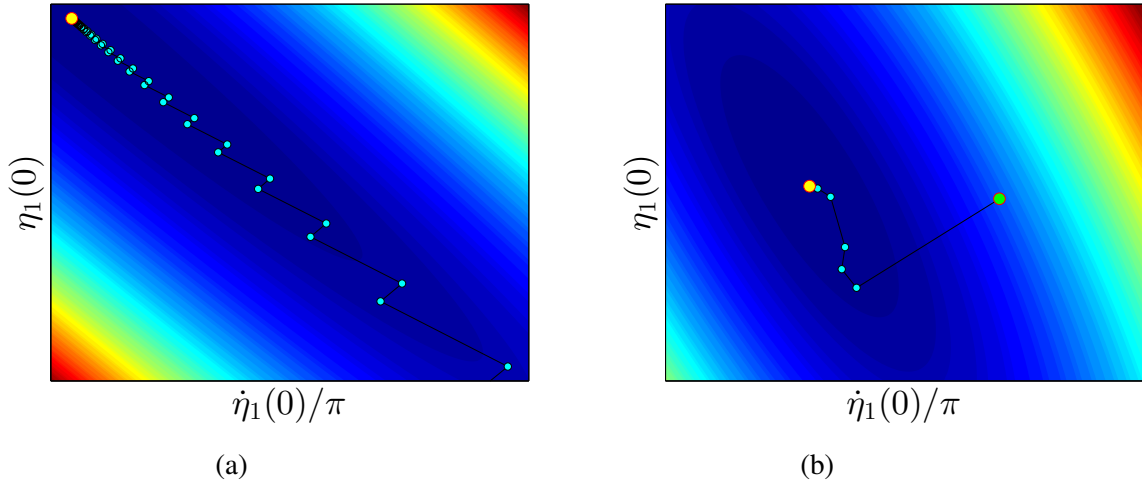
Figura 2.1 *Contour plots of the cost functional as a function of the initial condition of the first pressure and velocity mode. The yellow dot is the optimum. The cyan dots are associated with different steps of the gradient based optimisation loop. Figure (2.1a) is obtained with steepest descent update method while figure (2.1b) with conjugate gradient, which avoids zig-zagging.*

it is more efficient. The use of the steepest descent can cause the so called zig-zagging when the cost functional has the shape of a narrow valley. In this situation, the conjugate gradient converge drastically faster to the minimum because the direction of each step takes into account previous orientations. Figure (2.1a) and (2.1b) report the steps of the same optimisation problem, done with the steepest descent and the conjugate gradient method, respectively.

2.3   Tests for adjoint codes

Three main tests are performed to ensure that the adjoint equations are correctly implemented [46]:

1. Gradient Test (or Taylor test)

2. Tangent linear test (TLT)

3. Dot product test (DPT).

The TLT is used to test the tangent linear model (TLM), which, in turn, needs to be implemented to perform the dot product test, so, it can be seen as an auxiliary test.

2.3.1   Gradient test

In this section, the gradient test is explained by testing the Lorenz system. The gradient test consists of calculating $\nabla_{\mathbf{x}_0}(J)$ using a finite difference method and comparing it with the gradient provided by the adjoint algorithm. A set of perturbation amplitudes is chosen, for example $\varepsilon = \{10^{-1}, 10^{-2}, \ldots, 10^{-10}\}$, and each component of the gradient is computed for each of them as follows. The i-th component of the initial condition is perturbed using the current value of ε and the system is integrated over the time window. The solution is used to calculate a new $\tilde{J}_i$, where the subscript i means that is obtained perturbatig x_{i0} only. Let J be the cost functional calculated using the unperturbed initial condition $\mathbf{x}_0$, it follows that

$$\left(\frac{\partial J}{\partial x_{i0}}\right) = \frac{\tilde{J}_i - J}{\varepsilon} + O(\varepsilon) \ \text{ for } \varepsilon \to 0 \ . \tag{2.73}$$

Equation (2.73) provides an approximation of the derivative with an error of the same order of ε, so, if the adjoint algorithm provides the exact gradient, the difference $\alpha = \left(\frac{\partial J}{\partial x_{i0}}\right) - \left(\frac{\partial J}{\partial x_{i0}}\right)_{adj}$ must scales with ε. In other words, it has to be first order accurate. Such a behaviour can be readily checked by plotting α against ε using a loglog scale and observing an exact linearity with unitary slope, as shown in figure (2.2a).   The breakdown of the linearity for small values of ε is inevitable due to the error introduced by the floating point arithmetic in the numerical discretisation. It can be delayed reducing the time step (figure 2.3) and, more effectively, using higher order numerical scheme. Note that, if the numeric integration requires to compute more than one intermediate value of the function before moving to the next time step (e.g., 2th or 4th order Runge-Kutta), those exact same values must be used in the backward integration to compute the corresponding intermediate values of the adjoint variable. In this case the two numerical schemes are consistent. It can be done by storing them while marching forward or by calculating them again backward. Without this precaution, the gradient test would brake at much higher values of the perturbation's amplitude, introducing

(a)   (b)
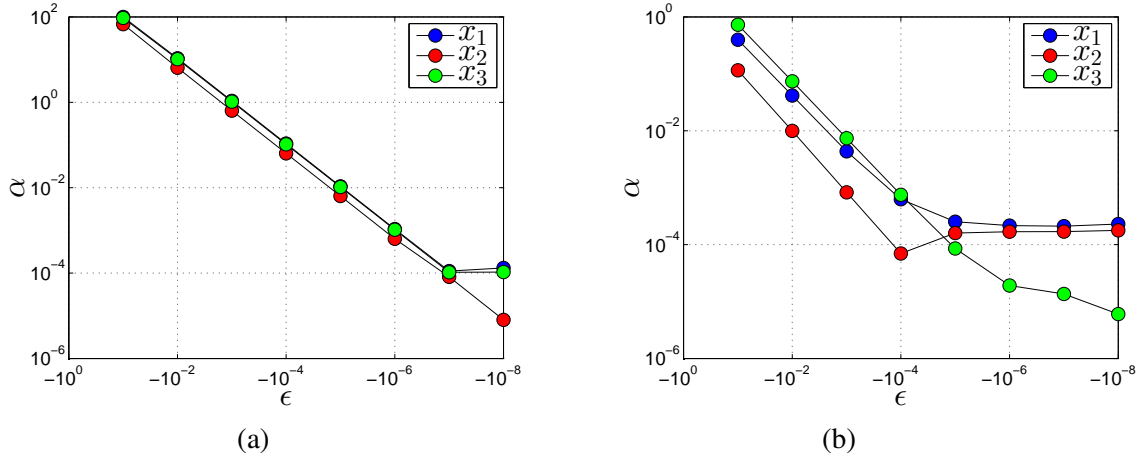
Figura 2.2 *Plots of the difference, α, between the approximated gradient in equation (2.73) and the one provided by the adjoint algorithm, against the perturbation amplitude, ε (gradient test). Different colors refer to the three components of the gradient, one for each dependent variable of the Lorenz system. The time step used is $dt = 10^{-3}$ and the time window is $t \in [0, 5]$. In figure (2.2a) the forward numerical scheme is consistent with the backward one, while in figure (2.2b) they are not consistent.*

eventually large error in the gradient, which would no longer be suitable for performing the minimization of the cost functional. In figure (2.2) the outcomes of the gradient test are compared changing the numerical scheme used for the backward adjoint integration. When it is not consistent with the forward scheme, (2.2b), the breakdown of linearity occurs for higher values of ε. In this case, forward and backward integrations are performed both using a 2nd order Runge-Kutta but the intermediate value that is calculated each time step is not exactly the same (i.e. the forward scheme is a Runge-Kutta *midpoint* and the backward is a *endpoint*).

When the test is performed on the thermoacoustic model introduced in section 2.1.3 of this chapter, one plot for each pressure and velocity mode is obtained. It is integrated using the more accurate 4th order R.-K., so the breakdown of the test occurs at lower values of ε. When the augmented system is considered, instead, the tests show smaller linear region in the $\alpha - \varepsilon$ plot, only for the adjoint parameters. It happens especially with β and τ, as shown in figure (2.4), while each ζ_j shows longer linear region (figure 2.5).

Such result is the reason why we performed dot-product test on the augmented system, which are reported in section 2.3.2. The outcome of the two tests are compared for both

(a) *Continuos adjoint, dt =10^{-3}.*

(b) *Continuos adjoint, dt =10^{-4}.*
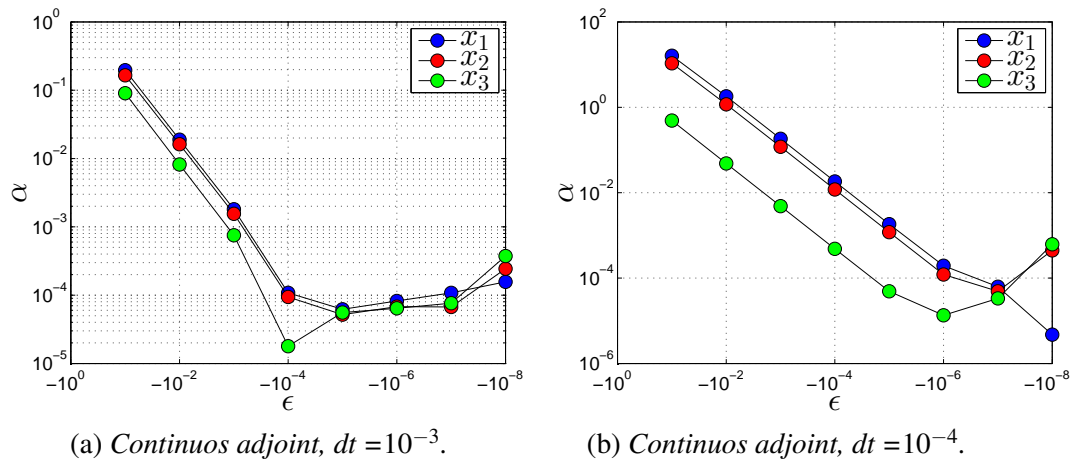
Figura 2.3 *Plots of α against ε (gradient test) for the Lorenz system. The continuous adjoint approach is employed. The time step is $dt = 10^{-3}$ in figure (2.3a) and $dt = 10^{-4}$ in figure (2.3b). Using a smaller time step results in a longer liner region of the plot, meaning that it increases the accuracy of the gradient computed with the CA.*

the Rijke tube's augmented model and the chaotic Lorenz system. It emerges from the comparison that, using the continuous adjoint, the DPT can be passed even if the gradient test shows a relatively short linear region, such as in figures (2.4a) and (2.4b).

(a) *Gradient test on τ, performed using dt=* 10^{-4}, $N_m = 3$, $\sigma_{pert} = 0.005$, $T_{fin} = 1.1$.

(b) *Gradient test on β, performed using* $dt = 10^{-3}$, $N_m = 3$, $\sigma_{pert} = 0.005$, $T_{fin} = 1$.

Figura 2.4
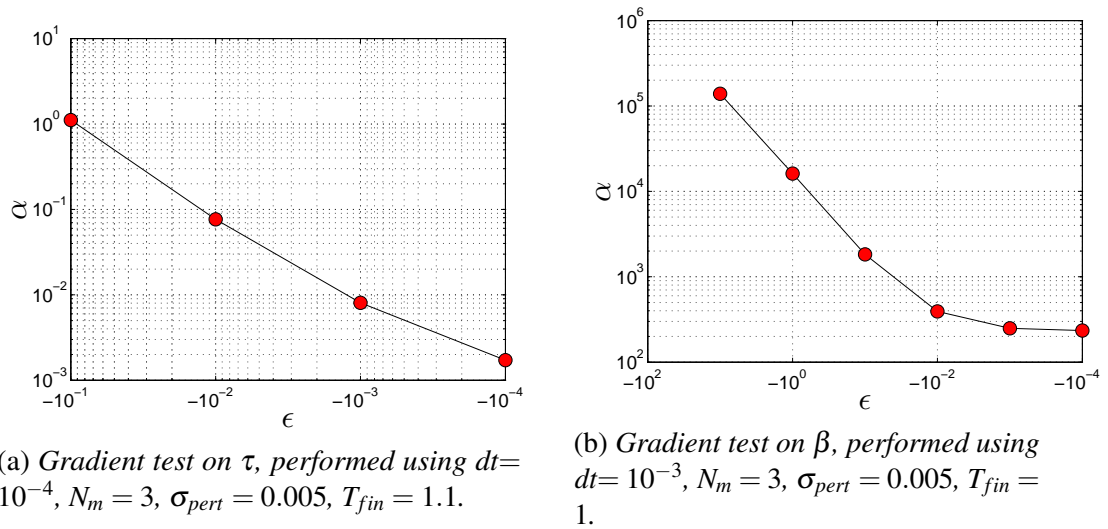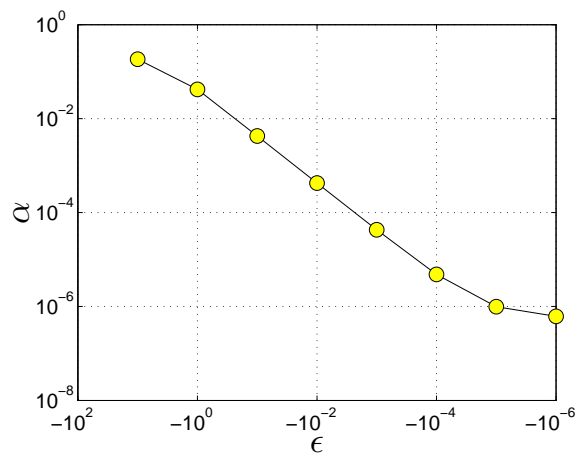
Figura 2.5 *Gradient test on ζ_2, performed using dt= 10^{-3}, $N_m = 3$, $\sigma_{pert} = 0.005$, $T_{fin} = 1$. The same test on ζ_1 and ζ_3 gives similar plots, which are not shown for brevity.*

2.3.2   Dot product test

In the section, the dot-product test is briefly introduced, then the tests are reported for the Lorenz system, the Rijke model and the Rijke model with state augmentation. When the latter is tested, we consider three augmented systems separately, one in which τ only is included into the augmented state vector, one in which β only is included and finally one in which ζ_j for $j = 1, \ldots, N_m$ are included.

Using a matrix notation, let $\mathbf{L}_k$ be the tangent linear operator of the system at hand (i.e. the operator associated with the TLM), $\delta \mathbf{x}_k$ the state vector and $\delta \mathbf{x}_k^+$ the adjoint state vector. The subscript k refers to the time step and the perturbation of a quantity is preceded by δ. Write

$$
\begin{aligned}
\delta \mathbf{x}_0^{\mathrm{T}} \delta \mathbf{x}_0^+ &= \delta \mathbf{x}_0^{\mathrm{T}} \left[\left(\mathbf{L}_N^{\mathrm{T}} \ldots \mathbf{L}_0^{\mathrm{T}} \right) \delta \mathbf{x}_N \right] \\
&= \left[\delta \mathbf{x}_0^{\mathrm{T}} \left(\mathbf{L}_N^{\mathrm{T}} \ldots \mathbf{L}_0^{\mathrm{T}} \right) \right] \delta \mathbf{x}_N \\
&= \left[\left(\mathbf{L}_N^{\mathrm{T}} \ldots \mathbf{L}_0^{\mathrm{T}} \right)^{\mathrm{T}} \delta \mathbf{x}_0 \right]^{\mathrm{T}} \delta \mathbf{x}_N \\
&= \left[\left(\mathbf{L}_N \ldots \mathbf{L}_0 \right) \delta \mathbf{x}_0 \right]^{\mathrm{T}} \delta \mathbf{x}_N \\
&= \delta \mathbf{x}_N^{\mathrm{T}} \delta \mathbf{x}_N.
\end{aligned}
\tag{2.74}
$$

Using the notation for continuous variables, t instead of k, it yields

$$
\delta \mathbf{x}^{\mathrm{T}}(0) \delta \mathbf{x}^+(0) = \delta \mathbf{x}(T) \delta \mathbf{x}(T)^{\mathrm{T}}.
\tag{2.75}
$$

The DPT consist of verifying the identity in equation (2.75) by calculating

$$
\Delta \overset{\mathrm{def}}{=} \delta \mathbf{x}(T) \delta \mathbf{x}(T)^{\mathrm{T}} - \delta \mathbf{x}(0) \delta \mathbf{x}^+(0),
\tag{2.76}
$$

where $\delta \mathbf{x}(0)$ is a randomly generated initial condition for the perturbation equations and $\mathbf{x}^+$ is the adjoint system's state vector. $\mathbf{x}^+(0)$ is obtained integrating the adjoint system from $t = T$ to $t = 0$, starting with the terminal condition $\mathbf{x}^+(T) = \delta \mathbf{x}(T)$. The RHS and LHS of

equation (2.75) are expected to match within machine accuracy when a discrete adjoint is used. For the continuous adjoint, such as the one employed here, it is acceptable to have a lower accuracy [45].

While the gradient test validates each adjoint variable separately, the DPT returns just a global number, as explained above, that accounts for all the adjoint variables. Therefore, we implement augmented systems that include in the state vector only one parameter at the time and we dot-test them. In principle, this could enable us to identify which adjoint parameter is the source of error in case the test does not pass. The adjoint of the Rijke equations (2.12), (2.13) and (2.14) returns an accurate gradient test. Similar results are obtained by testing each augmented system (i.e. the one including ζ_j, β and τ respectively). Interestingly, we observe that the discrepancies in the accuracy of the gradient test discussed before, between the thermoacoustic model and its augmented counterpart, are not reflected in the accuracy of the dot product test.

Testing the Lorenz system

The parameters, σ, ρ and β, are not included in the state vector (no state augmentation) and they are set equal to $10, 28$ and $8/3$ respectively, which generates a chaotic solution. The forward initegration scheme is a Runge-Kutta 2nd order (*midpoint*). Each test is performed by assigning the initial condition for the direct nonlinear integration using the Matlab function `normrnd(0,`σ_{Lor}`)`, which returns a pseudo-random value from a Gaussian probability distribution with zero mean and variance (σ_{Lor}^2). The perturbation initial condition, $\delta\mathbf{x}(0)$, is a 3-element vector of random numbers from a uniform probability distribution, ranged from 0 to 1, multiplied by a factor ε, as reported in table 2.1. The red term in table 2.1a stresses that one test returned a value of $\Delta = 10^{-1}$, which means that the test is not passed. The TLM diverged from the unperturbed trajectory, due to the fact that a large perturbation amplitude is employed, $\varepsilon = 10^{-1}$. Moreover, the continuous adjoint formulation is used, which is inherently less accurate. Note that, when a smaller time step is used, the tangent linear model does not diverge when $\varepsilon = 10^{-1}$ is employed.

Tabella 2.1 **Lorenz System**
The variance for the nonlinear initial condition is $var = 1$ and T_{fin} is equal to 1. The effect of var on the test is not investigated for this system, as it simply serves as a reference for the value of Δ. The test is run 10 times for each cases and the minimum and maximum values of Δ are reported.

(a) Continuous Adjoint			(b) Discrete adjoint		
dt	ε	Δ	dt	ε	Δ
10^{-3}	10^{-3}	$10^{-10} \div 10^{-14}$	10^{-3}	10^{-3}	$10^{-18} \div 10^{-21}$
	10^{-1}	$10^{-1} \div 10^{-10}$		10^{-1}	$10^{-14} \div 10^{-17}$
10^{-4}	10^{-3}	$10^{-8} \div 10^{-16}$	10^{-4}	10^{-3}	$10^{-17} \div 10^{-20}$
	10^{-1}	$10^{-9} \div 10^{-12}$		10^{-1}	$10^{-14} \div 10^{-16}$

Testing the thermoacoustic model

The numerical scheme used for time integration is a Runge-Kutta 4th order for both the direct and backward integrations. Each test is performed by assigning the initial condition, for the direct nonlinear integration, using the Matlab function `normrnd(0,`σ_{pert}`)`. It returns a random value from a Gaussian probability distribution with zero mean and given variance (σ_{pert}^2). It represents the initial perturbation that triggers the thermoacoustic oscillations. It has a great impact on the outcome of the dot product test, which becomes less accurate for higher values of σ_{pert}. The upper limit, after which the divergence of the linear perturbation is observed, is roughly $\sigma_{pert} = 1$. It does not represent a limitation because $\sigma_{pert} = 0.005$ is used in all the twin experimets reported in this work. The perturbation initial conditions, $\delta \mathbf{x}(0)$, is a $2N_m$-long vector of random numbers from a uniform probability distribution, ranged from 0 to 1. The outcome of the DPTs are reported in tables 2.2 to 2.5.

When the augmented system is considered, the length of the state vector changes according to the number of parameters concatenated to the Galerkin modes. $\delta \mathbf{x}(0)$ is then divided by its norm making it unitary, and it is finally multiplied by a factor ε. The more meaningful numbers reported in the tables above are coloured in cyan. That is because they are obtained by employing values of dt, $\sigma_{perturb}$ and N_{mod} corresponding to the ones used in the twin experiments discussed in the following chapter. As we can see, introducing the parameters in the state vector does not produce any negative effect on the dot-product test,

Tabella 2.2 **Rijke model**
The standard deviation of the initial condition is $\sigma_{pert} = 0.005$ because it is the value used for the twin experiments in data assimilation reported in this work (chapter 3). It is then increased to 0.5 in order to investigate the effects on the test's outcomes. $T_{fin} = 1$ as it is the length of the assimilation window in most of the cases. The test is run 10 times for each cases and the minimum and maximum values of Δ are reported.

(a) $N_m = 3$ (b) $N_m = 10$

dt	σ_{pert}	Δ	dt	σ_{pert}	Δ
10^{-3}	0.005	$10^{-14} \div 10^{-17}$	10^{-3}	0.005	$10^{-14} \div 10^{-15}$
	0.5	$10^{-12} \div 10^{-13}$		0.5	$10^{-11} \div 10^{-14}$
10^{-4}	0.005	$10^{-17} \div 10^{-18}$	10^{-4}	0.005	$10^{-16} \div 10^{-18}$
	0.5	$10^{-14} \div 10^{-16}$		0.5	$10^{-14} \div 10^{-15}$

Tabella 2.3 **Rijke model, augmented system with ζ_j for $j = 1, \cdots, N_m$**

(a) $N_m = 3$ (b) $N_m = 10$

dt	σ_{pert}	Δ	dt	σ_{pert}	Δ
10^{-3}	0.005	$10^{-14} \div 10^{-15}$	10^{-3}	0.005	$10^{-14} \div 10^{-15}$
	0.5	$10^{-12} \div 10^{-13}$		0.5	$10^{-11} \div 10^{-13}$
10^{-4}	0.005	$10^{-16} \div 10^{-18}$	10^{-4}	0.005	$10^{-16} \div 10^{-17}$
	0.5	$10^{-14} \div 10^{-15}$		0.5	$10^{-11} \div 10^{-15}$

Tabella 2.4 **Rijke model, augmented system with β**

(a) $N_m = 3$ (b) $N_m = 10$

dt	σ_{pert}	Δ	dt	σ_{pert}	Δ
10^{-3}	0.005	$10^{-14} \div 10^{-18}$	10^{-3}	0.005	$10^{-14} \div 10^{-15}$
	0.5	$10^{-12} \div 10^{-13}$		0.5	$10^{-10} \div 10^{-13}$
10^{-4}	0.005	$10^{-16} \div 10^{-18}$	10^{-4}	0.005	$10^{-16} \div 10^{-17}$
	0.5	$10^{-14} \div 10^{-16}$		0.5	$10^{-13} \div 10^{-16}$

proving that the adjoint equations are correctly derived and implemented.

Tabella 2.5 **Rijke model, augmented system with τ**

(a) $N_m = 3$			(b) $N_m = 10$		
dt	σ_{pert}	Δ	dt	σ_{pert}	Δ
10^{-3}	0.005	$10^{-14} \div 10^{-15}$	10^{-3}	0.005	$10^{-13} \div 10^{-15}$
	0.5	$10^{-11} \div 10^{-13}$		0.5	$10^{-9} \div 10^{-12}$
10^{-4}	0.005	$10^{-16} \div 10^{-17}$	10^{-4}	0.005	$10^{-15} \div 10^{-18}$
	0.5	$10^{-13} \div 10^{-15}$		0.5	$10^{-12} \div 10^{-14}$

2.4 Conclusions

In this chapter, we have introduced the thermoacoustic system with which we will work in the following chapter to perform data assimilation. It is shown that, once the pressure and the velocity perturbations are expanded in Galerkin modes, the system is reduced to a dynamical system with $2N_m$ degrees of freedom. Including the thermoacoustic parameters in the state vector, we obtain the augmented system and we derive the adjoint equations. They are used to compute the gradient of the acoustic energy at the final time, T, with respect to the initial conditions. The adjoint system of the Rijke model will be used to perform gradient based optimisation of the cost functional for data assimilation. For clarity, the terms in the derivation that change with the cost functional are coloured in cyan.

The application of the framework of data assimilation to thermoacoustic models has some differences with respect to its analogous in other fields, such as weather forecasting. Here, the physical time scales are shorter and the time intervals between two consecutive measurements can be of the order of the time step used for the discretisation of the assimilation window. Hence, observations can be obtained in continuous form (e.g. the analogical pressure signal recorded by a microphone) rather than at sparse set of instants. At the end of chapter 4, it will be discussed how this represents an advantage in terms of computational cost, only if the continuous adjoint approach is used. This is the reason why we choose the continuous adjoint approach.

Capitolo 3

Effect of the observations on state and parameter estimation

Introduction

The 4D-Var data assimilation problem can be cast as an optimization problem and it can be solved using a gradient based approach. We perform a series of data assimilation twin experiments, performing gradient based optimisation with the aid of adjoint equation (Lagrangian optimisation).

In this chapter, we report and comment on the results of a set of significant 4D-Var data assimilation twin experiments on the thermoacoustic model of a horizontal Rijke tube. First, it is shown how the number of computed acoustic modes affect the solution of the system and how the twin experiments are set up. Then, we describe the details of the cost functional specific to the thermoacoustic application of data assimilation. Finally, we show the effects on the analysis trajectory of the number of observations, their time distribution over the assimilation window and the frequency of observation.

3.1   Remarks on the thermoacoustic nonlinear dynamics

The thermoacoustic model consist of $2N_{mod}$ variables, which are the temporal evolution of the pressure and velocity mode amplitudes, while the spatial behaviour of pressure and velocity oscillations is assumed a priori when the Galerkin discretisation is performed (see section 2.1.3). The thermoacoustic system, when integrated, is initialized by imposing a non-equilibrium initial condition. Every variable starts oscillating as depicted in figure (3.1b) and (3.1a). The heat release term starts to oscillate as well, introducing energy in the system, which is dissipated by damping. In all the cases simulated in the present work, the long term solution shows that a balance is achieved between the energy input and output, leading to a limit cycle. The higher modes are associated with higher damping coefficients, so they approach a fixed point after few time units. As a result, for sufficiently large t, the solution is at regime and the trajectory obtained with 3 modes is qualitatively very similar to the one obtained setting $N_{mod} = 10$ because, in both cases, only the first three modes survives. What happens in the transient is of great interest. Here, the dynamics are unpredictable because of the complex mode interaction and we observe clearer differences when comparing the simulation with $N_m = 3$ (figure 3.1a), and the one with $N_m = 10$ (figure 3.1b). It will be shown how the process of data assimilation is affected by this behaviour, which characterises the physics underlying thermoacoustic instabilities. That is why, in all the twin experiments, the assimilation window starts at $t = 0$ and it is no longer than 2.5 time units. An exception is made in section 3.6.

3.2   Modelling observations: The twin experiment

We study the application of data assimilation to a thermoacoustic model without using real empirical data. The results discussed in the present work are the outcome of twin experiments. Twin experiments are the realisation of the method, often used in the framework of data assimilation, by which *synthetic* measurements are produced starting from the true system state. The latter is assumed to be known and it is produced by the model itself, in agreement with the strong constraint approximation (i.e. the model, in principle, can reproduce the true
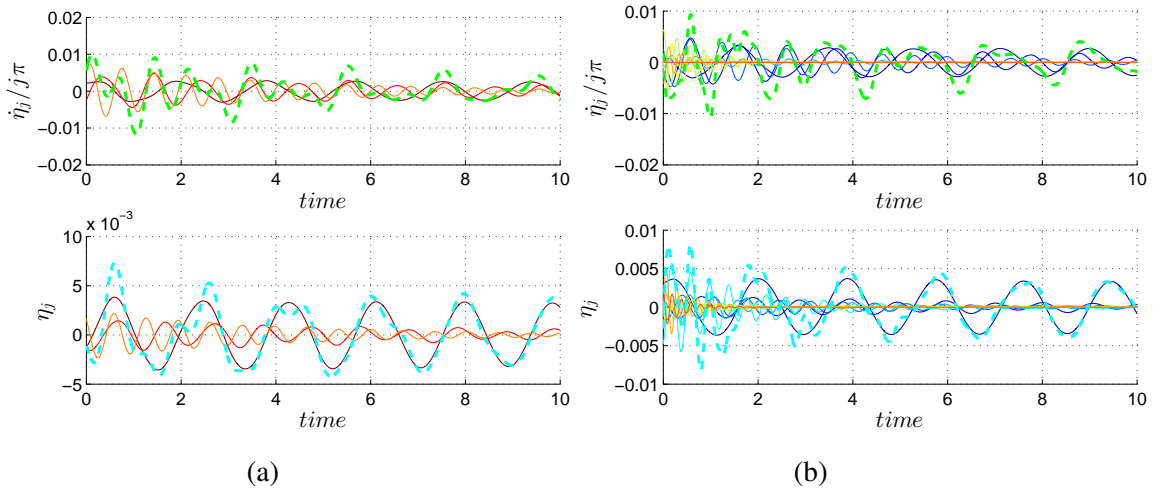
Figura 3.1 *Time series of the pressure (top) and velocity (bottom) modes, employing $N_{mod} = 3$ (3.1a) and $N_{mod} = 10$ (3.1b). The dashed lines are the global pressure (green) and velocity (cyan). The two cases are qualitatively similar for $t > 2$, while for $t < 2$ the dynamics are more complex in the case with 10 modes. The case with 3 modes, instead, shows patterns in the global pressure plot from the start.*

state of the system because the error is assumed to be in the initial conditions only and not in the equations).

The true state solution, $\mathbf{x}^{true}(t)$, is produced by perturbing the unstable fixed point at the origin of the phase space. Every dependent variable is initialised with a random value generated using the Matlab function `normrnd(0,`σ_{pert}`)`, which returns pseudo random numbers from the normal distribution with zero mean and variance equal to σ_{pert}^2. The background trajectory, $\mathbf{x}^{bg}(t)$, is obtained by perturbing each true mode initial condition and integrating the system again. This perturbation has zero mean and variance $\sigma_{bg}^2 = 20\sigma_{pert}^2$, where $\sigma_{pert} = 0.005$. The $i-$th observation about the global pressure, $p_{obs}^{(i)}$, is the true pressure plus a random error with zero mean and variance σ_{obs}^2. Future development of this work may include comparisons with an empirical data set. When working with real measurements, the true state is not known, so the background's initial conditions are obtained using a measurement at $t = 0$. That is why we choose to set $\sigma_{obs}^2 = \sigma_{bg}^2$.

Figure (3.2) shows how scattered the observations are using the values of σ_{obs} and σ_{bg} reported before. Despite this, the analysis pressure signal is a more accurate picture of the true pressure than the background is, revealing that the availability of unbiased measurements
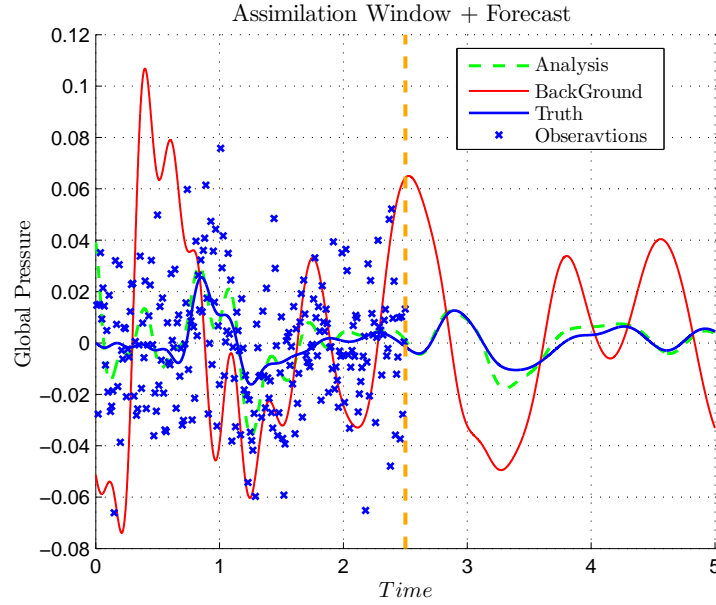
Figura 3.2 *Time series of the pressure. The observations, blue crosses, are produced using $\sigma^2_{obs} = 20\sigma^2_{pert} = 5 \cdot 10^{-4}$. This value of σ^2_{obs} produces very scattered measurements around the true pressure, and it is used in every twin experiment presented in this work.*

plays a crucial role in the assimilation process. It means that enough observations are available to ensure that only information about their mean value around the true state is assimilated.

Figure 3.3 shows the pressure error plot. The cyan vertical line indicates the end of the assimilation window, the red line is the difference between the true pressure and the background pressure, the green dashed line is the difference between the true pressure and the analysis pressure and the yellow dots are the difference between the true pressure and the measured pressure (at the time instants when observations are available). These quantities, normalized by the $p_0^{true} = p^{true}(t = 0)$, are referred to as background error, analysis error and observation error, respectively. The error plot provides an effective mean to assess the quality of the forecast by looking at the amplitude of the oscillations after the assimilation window. The quality of the background knowledge is improved by the assimilation process (*improved forecast*) when the amplitude of the oscillations of the green line are smaller than the ones of the red line. Figure (3.3a) and (3.3b) show that few measurements can be misleading. The optimal trajectory effectively minimises every measurement error and it is initialised close to
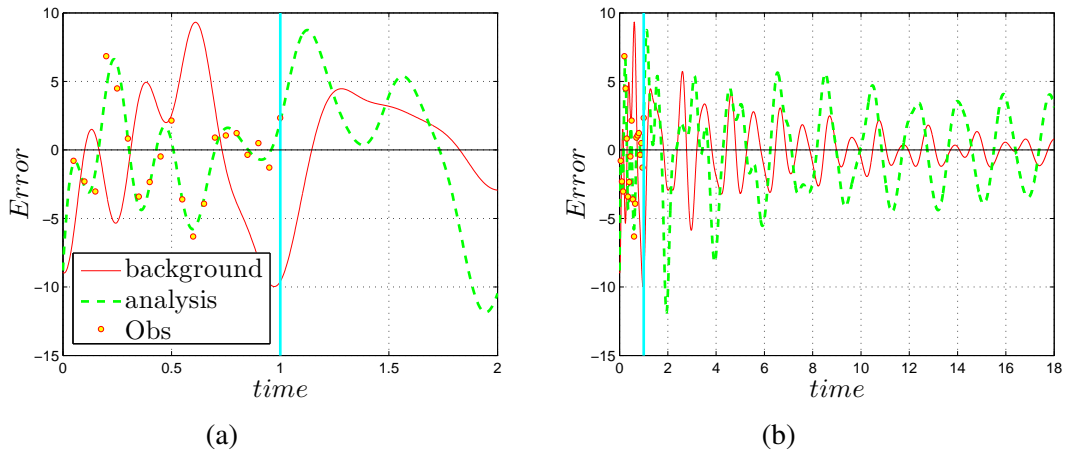
Figura 3.3 *Error plot of a twin experiment using $N_{obs} = 20$ and $N_m = 10$ zoomed in on the assimilation window (3.3a) and showing the extended forecast window (3.3b). Not enough observations are used to guarantee that information about their mean value only is assimilated, resulting in an analysis forecast with larger error peaks than the background forecast.*

$\mathbf{x}_0^{bg}$, resulting in a forecast where the optimal trajectory is less accurate than the background. Employing a lower number of modes or, equivalently, assimilating observations at regime, would reduce the chances to be inaccurate. It is due to the fact that the solution will have less degrees of freedom ($DOF = 2N_m$), therefore a more regular behaviour, and it will not be able to minimise the deviation from every observation. It can also be explained with the Shannon-Nyquist theorem (see subsection 3.19).

3.3   Cost functionals for state estimation

Optimisation problems are mainly characterised by the cost functional, as it is the mathematical expression of how information is measured. As seen in chapter 2, in data assimilation every contribution to J is weighted by the inverse of a covariance matrix. The higher the variance of a quantity, the smaller its weight. It means that we do not care about keeping the error low if the quantity in question is associated with high uncertainty. However, it is possible to value information in other ways. One way is by choosing an appropriate definition for the cost functional, leaving the covariance matrix unchanged.

3.3.1   Effect of the observation error

(a)

(b)

(c)

(d)
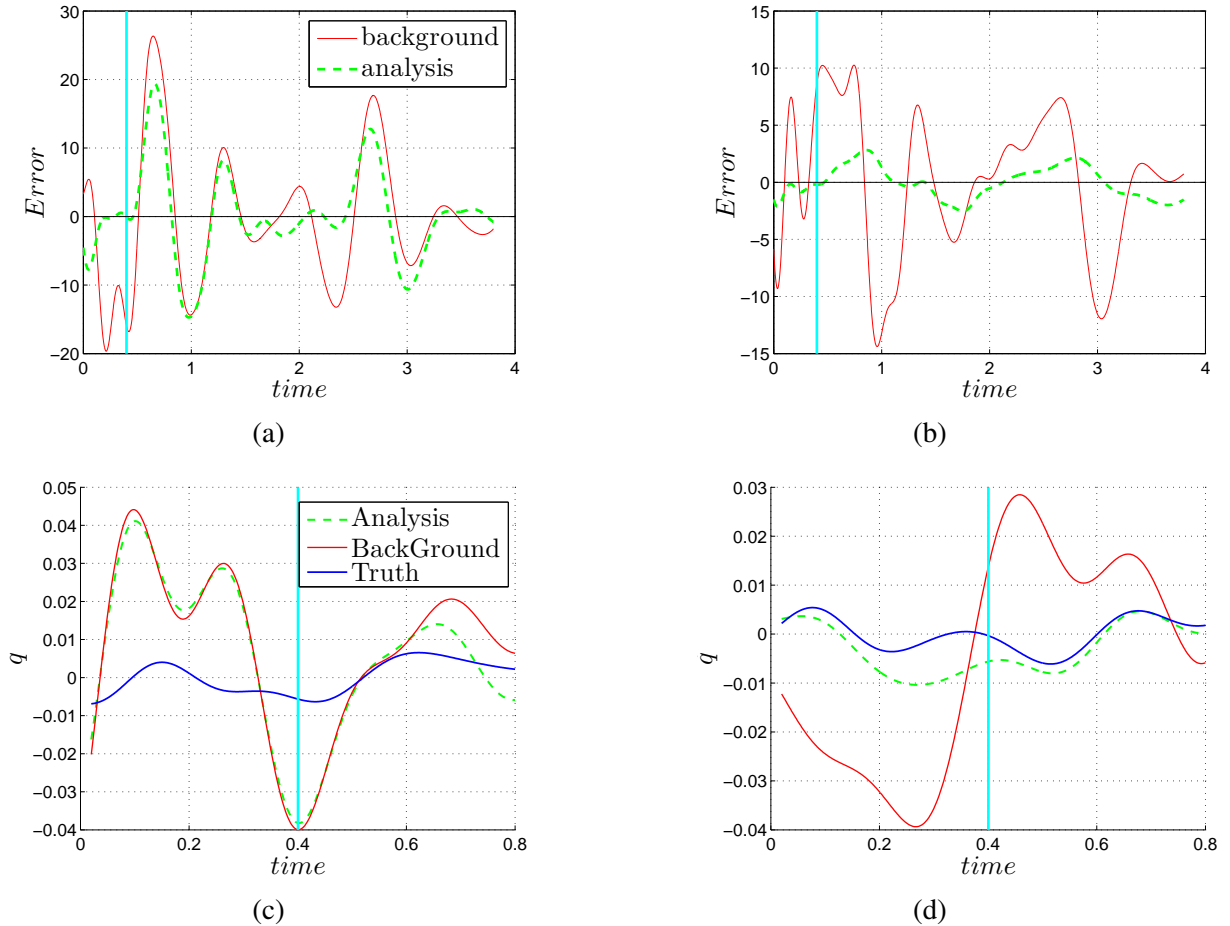
Figura 3.4 *Top: Time series of the background and analysis global pressure deviation from the true state. Bottom: Time series of the heat release term. On the left (3.4a and 3.4c) we model measurements on the pressure using J_{obs}^a. On the right (3.4b and 3.4d) measurements on each pressure modes are used, (J_{obs}^b), which provide an improved forecast.*

We can simulate two main scenarios. One in which the pressure measurements are on the global pressure, so we imagine having some empirical time series of *p*. The other scenario in which each pressure modes can be observed, or, similarly, the global pressure signal can be decomposed in modes, in analogy to what the model does. Figure (3.4a) is obtained using observations about the global pressure only. We can see that the analysis pressure error slightly deviates from zero in the time interval ranging from the first to the last observation. When the forecast window starts, the analysis suddenly approaches the background again.

Figure (3.4b) refers to the second scenario, so the observations contain information about every pressure modes. The forecast quality is considerably enhanced, also for the estimate of the heat release term, $\dot{Q}$ (see figures 3.4c and 3.4d). Note that the assimilation window is $T_{as} = 0.4$ and that 10 modes are computed. Under these circumstances, the observations are obtained during the transient, which lasts up to $t = 2$, approximatively, where the dynamics are unpredictable due to the interactions between many modes. As we will show in section 3.4, increasing N_{obs} is not an effective strategy to improve the forecast during the transient if the pressure only is observed. Figure 3.4 shows that decomposing the measured pressure signal into the natural acoustic modes is fundamental in the context of data assimilation in transient dynamics. From a numerical point of view, these two scenarios are modelled by changing J_{obs}, which can be defined as follows [1]

$$J_{obs}^a = \frac{1}{2R} \sum_{i=1}^{N_{obs}} \left(p(t_{obs}^i) - p_{obs}^{(i)} \right)^2 \qquad \text{for case in figure (3.4a), or} \qquad (3.1)$$

$$J_{obs}^b = \frac{1}{2R} \sum_{i=1}^{N_{obs}} \sum_{j=1}^{N_{mod}} \left\{ \left[\left(\frac{\dot{\eta}_j(t_{obs}^i)}{j\pi} \right) - \left(\frac{\dot{\eta}_j}{j\pi} \right)_{obs}^{(i)} \right] \sin(j\pi x) \right\}^2 \qquad \text{for case in figure (3.4b).}$$

$$(3.2)$$

Here x refers to the location where the measurament is taken and it is hidden in equation (3.1), as the term $\sin(j\pi x)$ appears in expression (2.11), when p is computed. t_{obs}^i is the instant at which the $i-$th observation is located. In the first case, the value of $p_{obs}^{(i)}$ is obtained by taking the pressure value given by the true solution, at the time step corresponding to the $i-th$ measurement, and adding a random error, with zero mean and variance equal to R. In the second case, each pressure mode observed, $\left(\frac{\dot{\eta}_j}{j\pi} \right)_{obs}^{(i)}$, is obtained in the same way, except

---

[1] It follows from the definition of J, given in chapter 2, that in the expression (3.1) R is a scalar and not a matrix, so its iverse is $1/R$. This comes from the fact that the measured quantity is a scalar (i.e. the global pressure). In expression (3.2), instead, the measured quantity is a vector made of all the pressure modes, so **R** is a covariance matrix. Here we assume that **R** is diagonal, and that the nonzero elements are all equal to R, yielding equation (3.2). This means we assume statistically independent errors.

that the error is added to each mode separately. The errors of the $i-$th observation are

$$J^a_{obs,i} = \frac{1}{2R}\left(p^{(i)} - p^{(i)}_{obs}\right)^2 \qquad \text{for case in figure (3.4a), and} \tag{3.3}$$

$$J^b_{obs,i} = \frac{1}{2R}\sum_{j=1}^{N_{mod}}\left\{\left[\left(\frac{\dot{\eta}_j}{j\pi}\right)^{(i)} - \left(\frac{\dot{\eta}_j}{j\pi}\right)^{(i)}_{obs}\right]\sin(j\pi x)\right\}^2 \qquad \text{for case in figure (3.4b).} \tag{3.4}$$

We calculate each $\nabla_{\mathbf{x}_0}(J_{obs,i})$ integrating the adjoint equations (2.55) to (2.62) backward, from $t = t_i$ to $t = 0$. Note that the terms in cyan in equations (2.57) and (2.60) must be changed according to the cost functional that we are using. Therefore, when equation (3.3) is used the coloured term in equation (2.57) and (2.60) are substituted by

$$\frac{\partial J^a_{obs,i}}{\partial \eta_j} = 0 \text{ and} \tag{3.5}$$

$$\frac{\partial J^a_{obs,i}}{\partial \frac{\dot{\eta}_j}{j\pi}} = \frac{1}{R}\left(p(t_i) - p^{(i)}_{obs}\right)\sin(j\pi x), \tag{3.6}$$

respectively. When equation (3.4) is used, the coloured term in equation (2.57) and (2.60) are substituted by

$$\frac{\partial J^b_{obs,i}}{\partial \eta_j} = 0 \text{ and} \tag{3.7}$$

$$\frac{\partial J^b_{obs,i}}{\partial \frac{\dot{\eta}_j}{j\pi}} = \frac{1}{R}\left[\left(\frac{\dot{\eta}_j(t_i)}{j\pi}\right) - \left(\frac{\dot{\eta}_j}{j\pi}\right)^{(i)}_{obs}\right]\sin^2(j\pi x), \tag{3.8}$$

respectively. The gradient of the total observation error is finally obtained as

$$\nabla_{\mathbf{x}_0}(J_{obs}) = \sum_{i=1}^{N_{obs}}\nabla_{\mathbf{x}_0}(J_{obs,i}), \tag{3.9}$$

which costs N_{obs} integrations each of them over the time interval $[0, t_i]$. Note that $\partial J_{obs,i}/\partial \eta_j$ is always zero as we are assuming that no data about the velocity is assimilated. From equations (3.5) and (3.7), it follows that the adjoint velocity, $\xi_j/j\pi$ for $j = 1, \ldots, N_{mod}$, is initialised with a zero terminal condition. It does not mean that $\partial J/\partial \eta_{j0}$ for $j = 1, \ldots, N_{mod}$ are zero, as they evolve from their terminal condition because the adjoint pressure modes, ν_j,

are initialized with a nonzero terminal condition.

Employing equation (3.2) sets a constraint that is more specific than using equation (3.1). In fact, the extremum of $J_{obs}^{(b)}$ will be associated with an analysis trajectory where every pressure mode contributes individually to minimise the penalty. Note also that the spatial phase of the modes is taken into account by the *sin* term, meaning that, if the measurement is taken close to a certain mode node, that contribution will have a small influence, and vice versa. If we observe the global pressure, we enforce the analysis trajectory to reproduce the true pressure level in the assimilation window (first scenario). However, the same pressure level is associated with multiple points in the phase space, meaning that two completely different trajectories can return the same pressure plot, especially when many modes are still active (transient dynamics). Data assimilation is an optimal blending of these observations with previous state estimate (background) to produce optimal initial conditions. As such, if we do not measure each mode deviation from the true solution, the outcome of the optimisation will be a solution that stays close to the true pressure in the assimilation window and that will stick to the background plot in the forecast.

3.3.2   Effect of the background error

The three cases reported in figure (3.5) show how the optimal solution is affected by the background term in the cost functional. Intuitively, the more the information from the background is valued (i.e. the higher its weight in the cost functional), the more our optimal solution will resemble the background rather than approaching the true state. This is true if observations are more accurate than the background knowledge. Therefore, what follows should be read as an overview of how the definition of J_{bg} affects the outcome of data assimilation. In real applications, we most likely will not have a perfectly unbiased pressure gauge. That is why considering the outcome of previous simulations (that is the background knowledge) can effectively improve the state estimation.

Numerically the background initial condition acts as an observation at time $t = 0$. As such, we assign a covariance matrix to it and we can decide to extract information about global

(a)

(b)

(c)
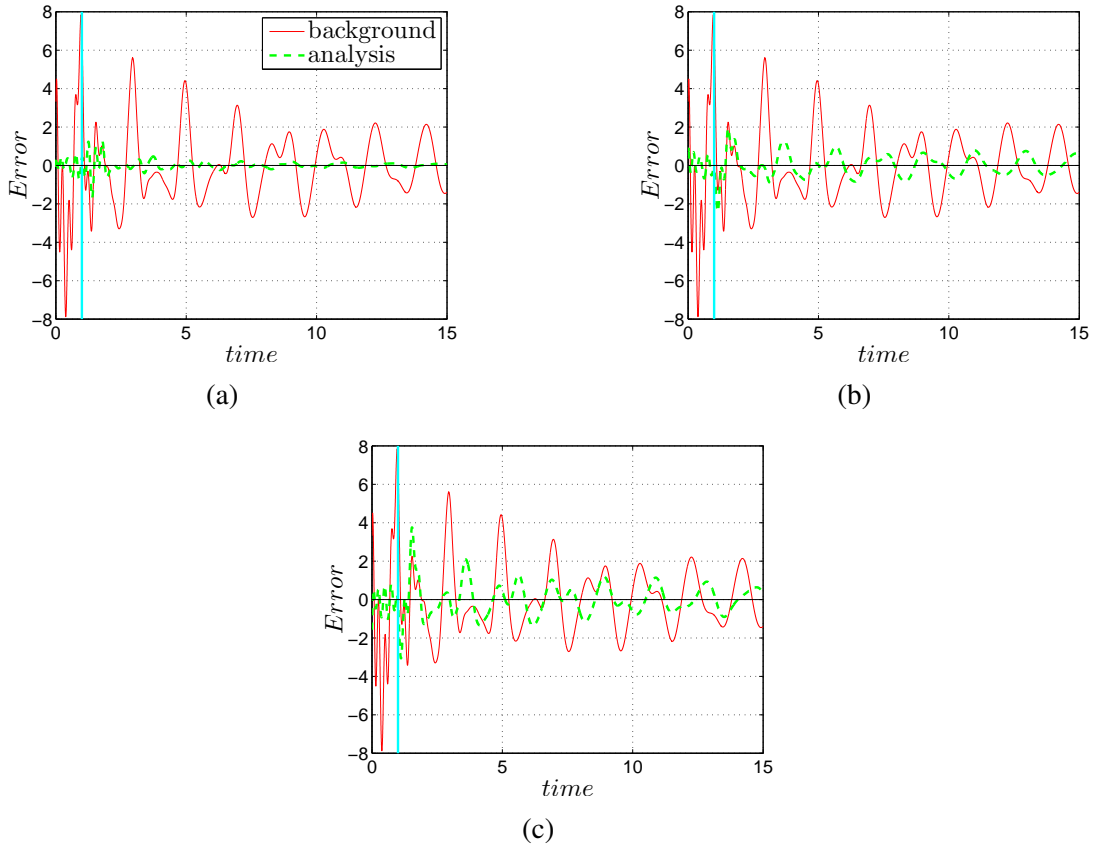
Figura 3.5 *Error plots using different background terms in the cost functional. Figure (3.5a), (3.5b) and (3.5c) are associated with J_{bg}^a, J_{bg}^b and J_{bg}^c, respectively. Observation error is measured using the cost functional J_{obs}^a. Case (3.5a) shows the smaller error peaks in the analysis forecast, therefore it is the best forecast. The opposite holds for case (3.5c).*

values, p and v, or about every single pressure and velocity mode[2]. The considerations made to understand the effect of J_{obs} and J_{bg} on the optimal state estimation are similar. When J_{bg} constrains every pressure mode, the analysis solution will stay closer to the background solution than the case in which the global pressure only is constrained.

Figures 3.5a, 3.5b and 3.5c are produced using different definitions for the cost functional

---

[2]Note that, in section 3.3.1, we did not consider the opportunity of having velocity measurements. We do so to further develop this work, which can include comparisons with an empirical campaign carried out using an experimental Rijke tube, which is equipped with pressure gauges only.

that measures the background error. They read[3]

$$J_{bg}^a = \frac{1}{2B} \sum_{j=1}^{N_{mod}} \left\{ \left[\left(\frac{\dot{\eta}_{j0}}{j\pi} \right) - \left(\frac{\dot{\eta}_{j0}}{j\pi} \right)_{bg} \right] \sin(j\pi x) \right\}^2, \qquad (3.10)$$

$$J_{bg}^b = \frac{1}{2B} \left(p(0) - p(0)_{bg} \right)^2 \text{ and} \qquad (3.11)$$

$$J_{bg}^c = \frac{1}{2B} \sum_{j=1}^{N_{mod}} \left[\left(\frac{\dot{\eta}_{j0}}{j\pi} \right) - \left(\frac{\dot{\eta}_{j0}}{j\pi} \right)_{bg} \right]^2 + \frac{1}{2B} \sum_{j=1}^{N_{mod}} \left[\eta_{j0} - \eta_{j0,bg} \right]^2 \qquad (3.12)$$

respectively. The number of observations, the background and the true system states are the same for all these cases. In close analogy with the cost functionals for the observations error, defined in the previous section, we can assimilate information about the global value of the pressure, (3.11), or about each single mode, (3.10). Equation (3.12) does not take into account the spatial behaviour of the solution. It stems from the fact that both terms are not multiplied by $\sin(j\pi x)$, so it has no clear correspondence in the empirical world. This is why it is not considered as a possibility for J_{obs}. We implement it for J_{bg} because, among the three of them, it is the case that gives the higher weight to J_{bg}, thus the one that value background information the most, followed by J_{bg}^a and finally J_{bg}^b, which is the one that values the background knowledge the least.

Comparing case (3.5c) with (3.5b) and case (3.5c) with (3.5a), the optimal solution that shows the larger peaks in the error plot is the one in case (3.5c). That is because it includes in the cost functional knowledge about (i.e. cost for) all the modes, velocity modes included. It therefore represents a strong constraint for the analysis trajectory to start close to the background and then follow it, in a space that is much more complex than the one depicted in the pressure plot or error plot. Looking at case (3.5a) and (3.5b), it appears that the background guess on the initial conditions of every pressure mode (case (3.5a)) was accurate enough. Therefore, employing J_{bg}^a instead of J_{bg}^b improves the analysis solution. In facts, it is like having an extra observation that gives information about all pressure modes and not about the pressure level only. Let us consider another case, where the background's knowledge is

---

[3]As in (3.2), equations (3.10) and (3.12) are derived under the assumption that **B** is diagonal, and that the nonzero elements are all equal to B.

poorer than the observations'. In such a situation, experiment (3.5a) is expected to produce a less accurate analysis than (3.5b), because too much importance would be given to an inaccurate information[4]. It emerges that it is better to have a *homogeneous* cost functional. It means that if the observations are all about the pressure, then J_{bg} should consider the pressure only. Velocity modes make half size of the state vector, so half of the dimensions of the phase space. It means that one can observe two similar pressure signals, which are produced by two trajectories that are considerably far away from each other. This possibility becomes more likely if a single constraint is set for the velocity modes, via J_{bg}^c, as in case (3.5c). On the other hand, data about the velocity can help, as long as they are enough to avoid that a case similar to the one in figure 3.3 happens. In other words, unbiased velocity measurements must be enough so that the information we get is about their mean value.

To compute the gradient of J_{bg} no integration of the adjoint equations is required because it encloses information about the state of the system at $t = 0$ (the initial conditions themselves). Its contribution to $\nabla_{\mathbf{x}_0}(J)$ appears in the cyan terms in equations (2.50) and (2.52). When J_{bg}^a is employed, they must be replaced by

$$\frac{\partial J_{bg}^a}{\partial \frac{\dot{\eta}_{j0}}{j\pi}} = \frac{1}{B}\left[\left(\frac{\dot{\eta}_{j0}}{j\pi}\right) - \left(\frac{\dot{\eta}_{j0}}{j\pi}\right)_{bg}\right]\sin^2(j\pi x) \text{ and} \tag{3.13}$$

$$\frac{\partial J_{bg}^a}{\partial \eta_{j0}} = 0, \tag{3.14}$$

respectively. When J_{bg}^b is employed, they must be replaced by

$$\frac{\partial J_{bg}^b}{\partial \frac{\dot{\eta}_{j0}}{j\pi}} = \left(p(0) - p(0)_{bg}\right)\sin(j\pi x) \text{ and} \tag{3.15}$$

$$\frac{\partial J_{bg}^b}{\partial \eta_{j0}} = 0, \tag{3.16}$$

respectively. Finally, when J_{bg}^c is employed, the cyan terms in equations (2.50) and (2.52)

---

[4] In principle, it is possible that case (3.5c) was better than, say, case (3.5b). It would have happened if, by chance, the background velocity modes had been initialised very close to the true initial state. In this case, giving such a knowledge a great weight in the cost functional would have resulted in a more accurate forecast, because the information would have been accurate.

must be replaced by

$$\frac{\partial J_{obs,i}^c}{\partial \frac{\dot{\eta}_{j0}}{j\pi}} = \frac{2}{B}\left[\left(\frac{\dot{\eta}_{j0}}{j\pi}\right) - \left(\frac{\dot{\eta}_{j0}}{j\pi}\right)_{bg}\right] \text{ and} \qquad (3.17)$$

$$\frac{\partial J_{bg}^c}{\partial \eta_{j0}} = \frac{2}{B}\left(\eta_{j0} - \eta_{j0,bg}\right), \qquad (3.18)$$

respectively.

3.4 Number of observations

As explained in section 3.2, there exists a lower limit for N_{obs} below which the observations affected by error can be misleading, producing an analysis trajectory that is less accurate than the background trajectory. In this section we discuss the effect of N_{obs} on the forecast quality working above that limit.

Generally speaking, the higher the number of unbiased observations the more the optimal solution will be similar to the true solution. This can be deduced by looking at figures (3.6a) and (3.6b). The value of N_{obs} is increased from 50 to 250, over an assimilation window of 2.5 time units, resulting in a smaller error amplitude when more observations are available. However, it is possible that increasing N_{obs} will not result in a better state estimation. This emerges while comparing figures (3.7a) and (3.7b), where no forecast improvement is visible due to a drastic increase in N_{obs}. This may seem counter-intuitive and it comes from two coexisting facts, namely that the assimilation window is in the transient ($T_{as} = 1$) and the fact that only the global pressure is observed. During the first time unit, when 10 modes are modelled, all of them are still active, that is when the system is observed here. As explained in section 3.3.1, measuring the global pressure there does not provide useful information to estimate the true system's state. Thus, we observe no forecast improvement here. When the assimilation window is extended up to 2.5 time units, instead, the global pressure is observed also when the dynamics is almost entirely characterised by the first two modes, that is in the last part of it. In this interval, data about the pressure level and knowledge about the
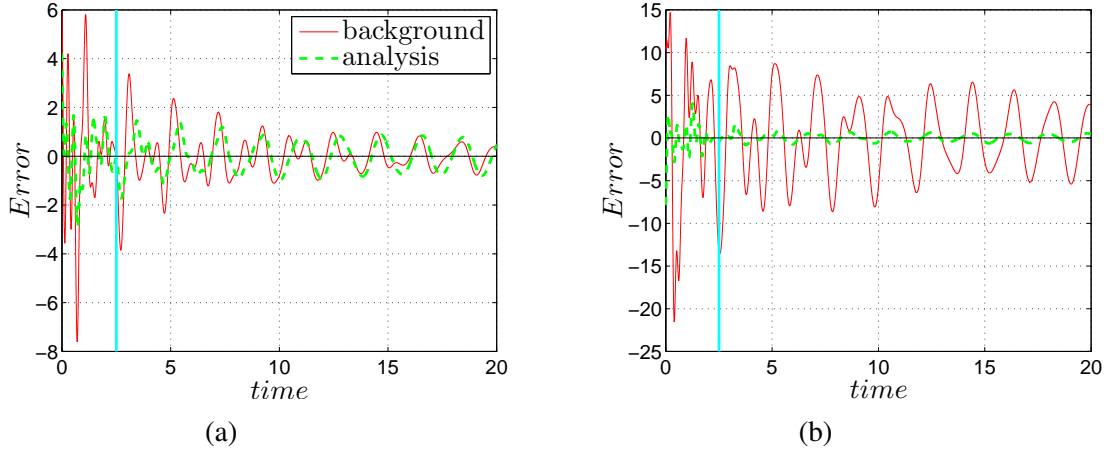
Figura 3.6 *Error plots of two different twin experiments. The assimilation window is 2.5 time units and the observation error is measured using J_{obs}^a in both cases. The choice of T_{as} implies that the system is observed also at regime. Case (3.6a) is obtained using $N_{obs} = 50$ and case (3.6b) using $N_{obs} = 250$.*

system state almost coincide. As a result, increasing the observation frequency produce a better forecast.

We conclude that, having poor information about the system's state (figure 3.6) can not be balanced simply by increasing the number of observations. Such a measure, in turn, considerably increases the computetional cost, so it must be avoided.

In the next section it is shown that there exists a limit for the measurement's frequency, after which no further forecast improvement is obtained by raising it.

3.5 Time distribution of observations

In this section two twin experiments are compared to investigate how the outcome of the assimilation process is influenced by the temporal distribution of the measurements. These simulations are set so that they share the true system's state and the background's initial conditions. The value of N_{obs} is also the same, equal to 100, as well as the time of the last observation available, which is at $t = 1$. The observations are on each pressure mode, so employing the cost functional J_{obs}^b .

In figure (3.8a) measuraments are evenly distributed over the assimilation window. In figure
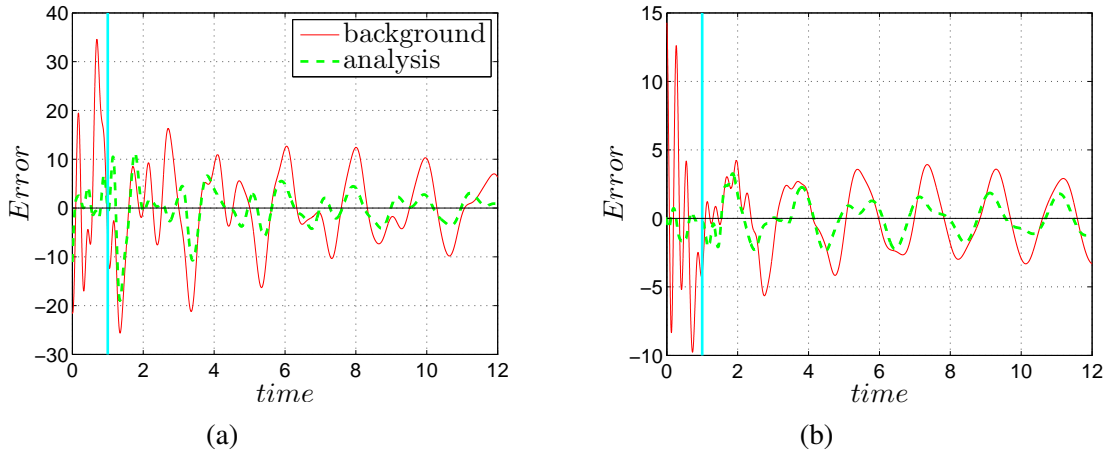
Figura 3.7 *Error plots of two different twin experiments. The assimilation window is 1 time unit and the observation error is measured using J_{obs}^a in both cases. The choice of T_{as} implies that the system is observed during the transient only. Case (3.7a) is obtained using $N_{obs} = 50$ and case (3.7b) using $N_{obs} = 250$.*

(3.8b) they are arranged in the last part of it, as close as possible to each other, that is every dt. It turns out from the look of the above mentioned figures, that a lower frequency of observation over a longer time interval is better than a high frequency over a short period. Moreover, the present comparison can help us understand if there exists a threshold value for the observation's frequency over which no valuable information is added for the state estimation. Results suggest that it exists. That can be explained by thinking that having an observation for each time step is still not enough to *push* the analysis trajectory close to the true solution. If such a threshold did not exist, setting the highest observation frequency over a shorter assimilation window would result in an analysis trajectory that passes close to the true trajectory in that time window. Then, the analysis solution would not diverge from the true solution. Working over such a frequency limit should be avoided, as it considerably increases the computational cost of the gradient computation. Indeed, each observation requires an adjoint integration, therefore the choice of N_{obs} should be weighed because it has a direct impact on the computational cost (see chapter 4 for more details on the topic).

Finally, we compare another couple of twin experiments with different time distributions of the observations like the ones in figures (3.8a) and (3.8b). This time we use the cost functional J_{obs}^a, which means that observations on the global pressure only are modelled. The

(a)   (b)
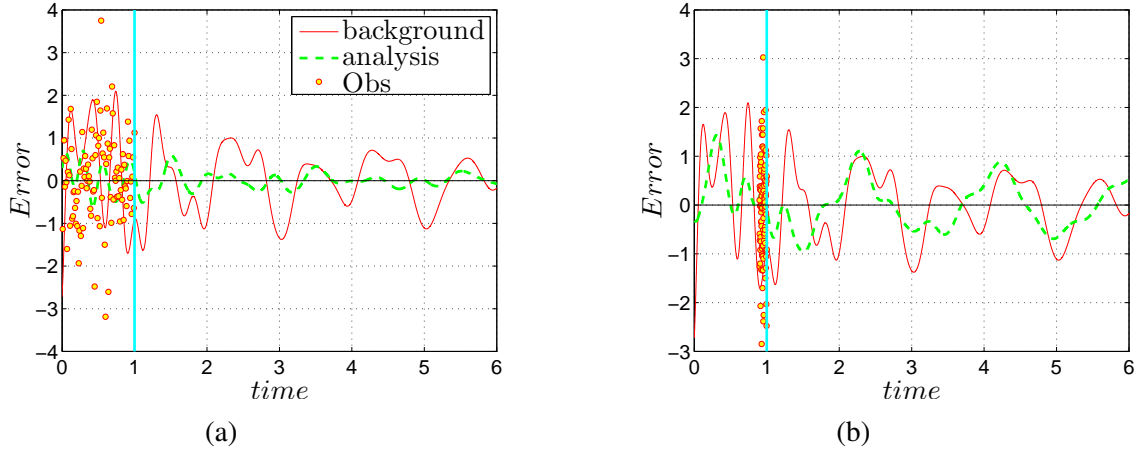
Figura 3.8 *Error plots of two different twin experiments. The assimilation window is 1 time unit, $N_{obs} = 100$ and the observation error is measured using J^b_{obs} in both cases. In case (3.8a) the measurements are evenly distributed over the assimilation window and in case (3.8b) they are arranged in the last part of it.*

same conclusions are drawn from this comparison, so the twin experiments are not reported for brevity.

3.6   Frequency of observations
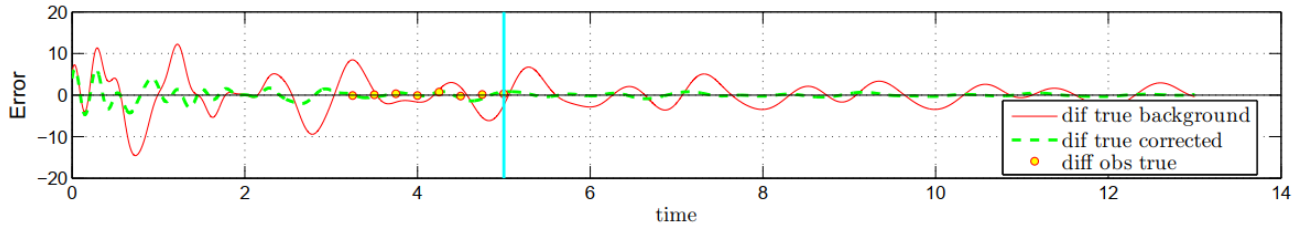
Figura 3.9 *Error plot obtained using $f_s = 8/2 > 6/2 = f_{max}$, thereby meeting the Shannon-Nyquist criteria to avoid aliasing.*

In section 3.1 it emerges that, at regime, the dynamics are dominated by the first 3 modes. As a result the last significant peak in the energy spectrum has the same frequency of the 3rd mode, that is $f_{max} = f_3 = \frac{N_m \pi}{2\pi} = \frac{3}{2}$. We show here that, in agreement with the
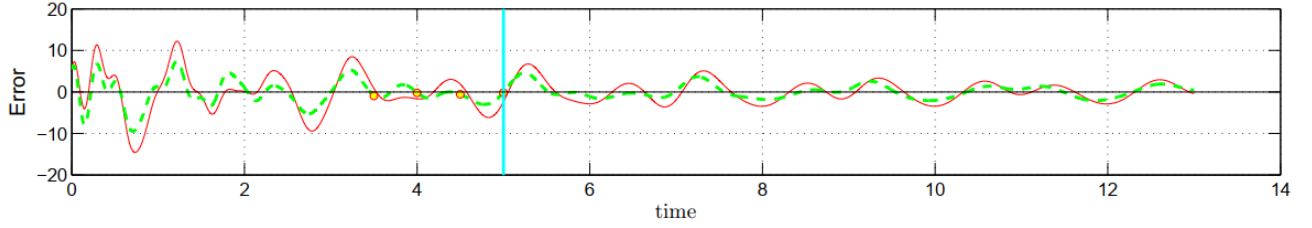
Figura 3.10 *Error plot obtained using $f_s = 4/2 < 6/2 = f_{max}$, thereby not meeting the Shannon-Nyquist criteria.*

Shannon-Nyquist criteria, it is necessary to have a frequency of observations, f_s, that is

$$f_s > 2f_{max} \tag{3.19}$$

in order to see an improvement in the forecast (see figure 3.9). On the other hand, figure 3.10 shows that, if the condition in equation (3.19) is not met, no forecast improvement is observed. Note that the Shannon-Nyquist theorem does not consider the possibility for the observations to be affected by error. Therefore, the value of σ_{obs} used to produce the aforementioned figures, is reduced by two order of magnitude, becoming negligible.

3.7 Conclusions

This chapter examines the outcome of 4D-Var data assimilation twin experiments on a low-order thermoacoustic model. We use the first 10 natural acoustic modes of the Rijke tube to capture the transient dynamics, and we observe that the outcome of the assimilation process strongly depends on whether or not we assimilate data in the transient or at regime. Measuring the pressure during the transient does not improve the forecast, regardless of the frequency of observation. Therefore, we propose a more effective cost functional which sets a constraint for each natural pressure mode of the duct. Employing this cost functional produces improved forecast also during the transient, as it captures the dynamics of every mode.

Different number of observations are employed to confirm that more measurements are associated with a better forecast. It is also shown that it is better to have a uniform distribution

of the observation over the assimilation window to reduce the error of the analysis prediction. Finally, we study the affect of the frequency of observations at regime. It emerges that a low observation frequency can be employed when few modes are active, providing accurate forecast, as a consequence of the Shannon-Nyquist theorem. It is very important for real application because a low observation frequency requires low computational cost, enabling data-based real-time calibration of low-order thermoacoustic models.

Capitolo 4

Computational cost of data assimilation

Introduction

In this chapter, it is shown that the computational cost of 4D-Var data assimilation is determined by the cost functional definition, the degrees of freedom of the model and the method used for the gradient computation (i.e. continuous adjoint, discrete adjoint or finite difference). In section 4.1 some key differences between the continuous (CA) and discrete adjoint (DA) are described by referring to the Lorenz system. It emerges that the computational cost to obtain gradient information can vary depending on which approach is used.

In section 4.3 we show how to calculate the number of floating-point operations (*flops*) needed to compute the gradient in the framework of data assimilation using (i) the method employed in the present work, that is the CA, and using (ii) the direct sensitivity analysis (finite difference method). Finally, we justify the choice of using the continuous adjoint method with a view to future development of this work, based on the conclusions of section 4.1.

4.1   Notes on the discrete and continuous adjoint (applied to the Lorenz system)

To derive the adjoint of a nonlinear system, the latter must be linearised. It can be done with a continuous approach (CA) or with a discrete one (DA). In both cases, the final target is to obtain gradient information of a given cost functional J at a certain final time $t = T$, with respect to the initial conditions, $\mathbf{x}_0 = \mathbf{x}(0)$. Among others, J can have one of the following features:

- be a continuous function of the system state vector $\mathbf{x}(t)$ for $t \in [0, T]$, e.g.

$$J = \frac{1}{T} \int_0^T ||\mathbf{x}(t)||^2 \, dt \; ; \tag{4.1}$$

- be a function of $\mathbf{x}(t)$ for $t = T$ only or for $t = T$ and $t = 0$, e.g.

$$J = \frac{||\mathbf{x}(T)||^2}{||\mathbf{x}_0||^2} \; . \tag{4.2}$$

The vector $\mathbf{x}$ is the state vector, which is $\mathbf{x} = [x_1, x_2, x_3]$ for the Lorenz system, which is being introduced soon. In the following two subsections, it is explained why the computational cost to obtain the gradient depends on which approach is considered between CA and DA. Specifically, we show that, using the cost functional defined in equation (4.1), the continuous approach is cheaper.

   We do so by referring to the Lorenz system because it is smaller than the thermoacoustic model of the Rijke tube, making the exposition of the equations less cumbersome. The Lorenz equations are given by the nonlinear system [47]:

$$\begin{cases} \dfrac{dx_1}{dt} = -\sigma x_1 + \sigma x_2 \\ \dfrac{dx_2}{dt} = \rho x_1 - x_2 - x_1 x_3 \\ \dfrac{dx_3}{dt} = x_1 x_2 - \beta x_3 \end{cases} \tag{4.3}$$

where x_1, x_2 and x_3 are function of time and σ, ρ and β are parameters. Their values are set to $10, 28$ and $8/3$ respectively, which gives a chaotic solution.

4.1.1   Continuous approach

As shown in chapter 2, when the continuous approach is used we linearise an auxiliary functional called Lagrangian, $\mathscr{L}$, rather than just the system alone. The Lagragian contains both the direct system, in the form of constrains, and the expression of the cost functional as a function of the system's state vector. As a reference, the expression of the cost functional in the Lagrangian is the analogous of the first term in the RHS of equation (2.39). When the linearization is performed and the condition to find an extremum of the Lagrangian are imposed, the CA produces the so-called adjoint system. The adjoint of the Lorenz system, associated with J defined by equation (4.1), reads

$$
\begin{cases}
\dfrac{da_1}{dt} = \sigma a_1 - \rho a_2 + a_2 x_3 - a_3 x_2 - \textcolor{blue}{x_1} \\
\dfrac{da_2}{dt} = -\sigma a_1 + a_2 - a_3 x_1 - \textcolor{blue}{x_2} \\
\dfrac{da_3}{dt} = \beta a_3 + a_2 x_1 - \textcolor{blue}{x_3}
\end{cases}
\tag{4.4}
$$

where a_1, a_2 and a_3 are the Lagrange multipliers of x_1, x_2 and x_3 respectively. It is derived in analogy with the procedure shown in chapter 2, section 2.

The blue terms appear in the adjoint equations because the terms associated with the cost functional in the Lagrangian are a function of t for $t \in [0, T]$. If the cost functional defined by equation (4.2) is used, the blue terms are equal to zero. Many different cost functionals of the type in equation (4.2) can be defined. What could change from one to another are just the equations for the gradient information (the analogous of equations 2.50 to 2.54) and the terminal conditions for the adjoint variables.

For both the cost functionals, the gradient information can be computed at the cost of one forward and one backward integration over the time interval $[0, T]$. The reason why the computational cost remains unchanged is that the continuous approach can include

information of the cost functional into the adjoint system (the blue forcing term), as long as J has a continuous mathematical espression, which is also differentiable.

4.1.2 Discrete approach

The derivation of the discrete adjoint for the Lorenz equations goes beyond the purpose of this thesis. The reader can refer to [45] and [46] for an introduction to discrete adjoint problems. The DA can provide the gradient for both kinds of cost functionals as well. However, the discrete adjoint equations do not take into account how J is defined, so they don't show any forcing term in case J is chosen according to equation (4.1). It means that the discrete adjoint equations are unchanged regardless of the choice of J. The cost functional in equation (4.1) is treated as it was

$$J = \int_0^T \frac{||\mathbf{x}(t)||^2}{T} \, dt \approx \sum_{k=1}^{N_{step}} \frac{||\mathbf{x}_k||^2}{T} \, dt \ , \tag{4.5}$$

where $\mathbf{x}_k = \mathbf{x}(t_k)$. By defining $||\mathbf{x}_k||^2/T = J_k$, we obtain

$$J \approx dt \sum_{k=1}^{N_{step}} J_k \ , \tag{4.6}$$

where N_{step} is the number of time steps, dt, in which the interval $[0,T]$ has been discretised, and t_k is the time at the k-th step. The computational cost that is necessary to calculate $\nabla_{\mathbf{x}_0} J$ has increased compared to the CA since now the problem is posed as if N_{step} cost functionals were to be considered. The number of backward integrations rises up to N_{step}, each of them over a time interval $[0,t_k]$. That is because no Lagrangian has been defined and the direct system only has been linearised, yelding the tangent linear model (TLM, see appendix B). Using the cost functional defined according to equation (4.2) the discrete approach can compute the gradient performing one adjoint integration, so, in this case, the CA and the DA are equivalent in terms of computational cost. The reason is that k takes only one value in equation (4.6), namely $k = N_{step}$.

4.2   The cost functional in data assimilation

The cost functional traditionally encountered in the framework of data assimilation can be written as

$$J = J_{bg} + J_{obs}. \tag{4.7}$$

In particular, for J_{bg} we make use of one of those reported in equations (3.10) to (3.12), while for J_{obs} we use equation (3.1) or (3.2), which are reported here again for convenience. They read

$$J_{obs}^a = \frac{1}{2R} \sum_{i=1}^{N_{obs}} \left(p(t_{obs}^i) - p_{obs}^{(i)} \right)^2, \tag{4.8}$$

$$J_{obs}^b = \frac{1}{2R} \sum_{i=1}^{N_{obs}} \sum_{j=1}^{N_{mod}} \left\{ \left[\left(\frac{\dot{\eta}_j(t_{obs}^i)}{j\pi} \right) - \left(\frac{\dot{\eta}_j}{j\pi} \right)_{obs}^{(i)} \right] \sin(j\pi x) \right\}^2. \tag{4.9}$$

The computation of the gradient of J_{bg} does not require any model integration because they are quantities that depend on $\mathbf{x}(0) = \mathbf{x}_0$ only. Looking at the expressions for J_{obs} we see that, in both cases, they are a function of the system state vector at N_{obs} different instants in time. These are t_{obs}^i, which are the points of the time axes at which the i-th observation is taken. The sensitivity of J_{obs} with respect to the initial conditions of the system is calculated as a sum of N_{obs} sensitivities, $\nabla_{\mathbf{x}_0}(J_{obs,i})$, one for each measurement. Therefore, to calculate

$$\nabla_{\mathbf{x}_0}(J_{obs}) = \sum_{i=1}^{N_{obs}} \nabla_{\mathbf{x}_0}(J_{obs,i}), \tag{4.10}$$

N_{obs} adjoint integrations must be performed, each of them over the time interval $[0, t_i]$. It holds for both the CA and the DA, so the computational cost to perform data assimilation twin experiments with the CA is the same as with the DA. The reason is that the cost functionals in equations (4.8) and (4.9) are equivalent to N_{obs} cost functionals of the type in equation (4.2). Thus, the capability of including information about the cost functional into the adjoint equations, that characterises the continuous approach and that is discussed in subsection

4.1.1, can not be exploited when cost functionals such as the ones used in data assimilations are employed.

4.3 Forward and adjoint gradient computations in data assimilation
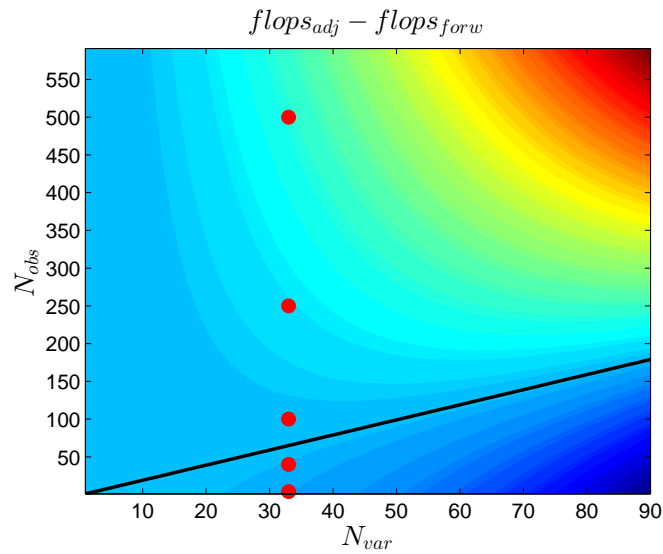
Figura 4.1 *Contour plot of the difference between $flops_{adj}$ and $flops_{forw}$, the black line is the dividing line described in eq. (4.17). Above that line, the adjoint method is not the cheapest if compared with the forward sensitivity analysis. The number of variables refers to a case in which 10 modes are considered and it is computed according to equation (4.11)*

It has been shown that CA and DA have the same computational cost, as a result of how J_{obs} is defined in the data assimilation framework. Therefore, adjoint sensitivity is compared here to the forward senitivity, with no need to specify if CA or DA is employed. In this section some practical examples are used to show when an adjoint sensitivity analysis is more convenient than a forward one. The system considered is the augmented thermoacoustic model of a Rijke tube, discretized in Galerkin modes, that is introduced in chapter 2. When the augmented state is considered, the size of the system is

$$N_{var} = 3N_m + N_{param} \, ,$$

(4.11)

where N_{param} is the number of parameters included into the augmented state vector. The computational cost of one forward integration is equal to

$$flops_{int} = N_{var}^2 N_{step} \,, \tag{4.12}$$

where $flop$ stands for "Floating-Point Operations". The cost of a backward integration is the same. Assuming that the observations are equally spaced in time, and calling N_{step}^i the number of time steps in the interval $[0, t_{obs}^i]$, the $flops$ necessary to obtain $\nabla_{\mathbf{x}_0} J$ are equal to

$$flops_{adj} = \sum_{i=1}^{N_{obs}} N_{var}^2 N_{step}^i \,, \tag{4.13}$$

where

$$N_{step}^i = N_{step} \frac{i}{N_{obs}}. \tag{4.14}$$

Note that N_{step}/N_m is an integer under the assumption of equally spaced observations in time. Substituting equation (4.14) in equation (4.13), it yields $flops_{adj} = \dfrac{N_{var}^2 N_{step}}{N_{obs}} \sum_{i=1}^{N_{obs}} i.$ The summation term is $\sum_{i=1}^{N_{obs}} i = \dfrac{N_{obs}^2}{2} + \dfrac{N_{obs}}{2}$. Finally, equation (4.13) can be written as

$$flops_{adj} = N_{var}^2 N_{step} \left(\frac{N_{obs}}{2} + \frac{1}{2} \right) \,. \tag{4.15}$$

The forward sensitivity analysis requires the direct system to be integrated N_{var} times, yielding

$$flops_{forw} = N_{step} N_{var}^3 \,. \tag{4.16}$$

The difference between equation (4.15) and (4.16) is set to zero to determine the condition in which $flops_{adj} = flops_{forw}$. This condition is not dependent of the number of time steps,

and, assuming $N_{obs} >> 1$, it reads

$$N_{var} \approx \frac{N_{obs}}{2} \; .$$

<div align="right">(4.17)</div>

Equation (4.17) is a straight line in the $N_{var} - N_{obs}$ plane (black line in figure 4.1), and each twin experiment can be represented as a dot on the same plane (red dots in figure 4.1). For the dots below that line $flops_{adj} < flops_{forw}$, therefore the adjoint sensitivity is computationally cheaper. The opposite holds for the points above that line.

Figure (4.1) shows the contour of $flops_{adj} - flops_{forw}$ for a fixed $N_{step} = 10^3$. The red dots refer to the number of variables of the augmented state system, calculated by using equation (4.11), where $N_{param} = 3$. N_{obs} refers to the number of observations we used to perform twin experiments, some of which are commented in chapter 3. The contour plot has a qualitative meaning because the cases plotted do not share the same value of N_{step}. However, as already said, the equation of the black line (4.17) does not depend on N_{step}. It means that, for the cases below that line, the adjoint sensitivity is computationally cheaper than the forward sensitivity, and vice versa.

4.3.1 Future work

The CA approach can encapsulate information about the cost functional into the adjoint equations via the forcing terms (blue terms in equations 4.4). This happens when J is a continuous function of time, which is not the case for the cost functionals used in data assimilation, presented in section 4.2. As already discussed in section 2.4, in thermoacoustic applications the time interval between two consecutive observations can be of the order of the time step used for the discretisation of the assimilation window. This fact suggests that a continuous formulation for J_{obs} can be used. The main advantage of doing that would be a reduction of the computational cost to calculate $\nabla_{\mathbf{x}_0} J$, as it reduces, from N_{obs} to 1, the number of integrations of the continuous adjoint equations. We present here a possible development of this work that will make use of such a feature of the continuous formulation.

In practice, when the pressure signal is captured by a pressure gauge, what we obtain is a sampled signal with a given sampling frequency. According to the Nyquist-Shannon criterion, the sampling frequency must be at least twice as the highest frequency in the spectrum of the signal that we are interested in. Performing a discrete Fourier transform (DFT), the measured pressure can be expressed by a truncated Fourier expansion. It means that our measurements can be written in the form of continuous functions (summation of sines and cosines) defined over the time interval $[0, T]$. The cost functional associated with the observations, J_{obs}, is then expressed as the difference of the measured Fourier modes and the variables of the thermoacoustic model (Galerkin modes, which are Fourier modes). At this stage, J_{obs} is another continuous function defined in $[0, T]$ and becomes the one defined in equation (4.1). Defining $J_{obs}(t)$ for $t \in [0, T]$ allows us to run a single adjoint integration to compute its gradient with respect to the initial conditions. Note also that the need for a single adjoint integration to compute the gradient makes the the adjoint method always cheaper than the forward gradient computation ($flops_{adj} < flops_{forw}$). Moreover, we set a constraint mode by mode, in close analogy with what the cost functional in equation (3.2) does. As discussed in subsection (3.3.1), that cost functional can capture the transient dynamics of the thermoacoustic oscillations, when many modes are interacting with each other. This complexity is one of the distinctive characteristics of the physics underlying thermoacoustic instabilities, so it is fundamental to be able to improve the forecast under these conditions at a low computational cost.

4.4   Conclusions

First, two kinds of cost functionals were introduced, one that is defined over a time interval (see equation 4.1) and the other that is pointwise defined (see equation 4.2). The cost functional that is typical of data assimilation is the latter, for which $\nabla_{\mathbf{x}_0} J$ can be calculated using the CA or the DA at the same computational cost. Secondly, we provide a framework to assess whether it is cheaper to compute $\nabla_{\mathbf{x}_0} J$ using a forward scheme or an adjoint scheme based on the number of observations and the number of Galerkin modes. It emerges that the

answer is not obvious, depending on the case at hand. Finally, an outlook on future work is reported, which provides also a guideline for the choice of the continuous adjoint approach in this work: Based on the conclusions in sections 4.1 and 4.3, the CA is the cheapest method in terms of computational cost. To perform real-time calibration of thermacoustic models it is crucial to develop efficient and fast algorithms. For this reason the approach used in this work, the continuous adjoint, is the most convenient.

References

1   A. P. Dowling and A. S. Morgans. Feedback control of combustion oscillations. Annual Review of Fluid Mechanics, 37:151-182, 2005.

2   A. P. Dowling and J. E. Ffowcs Williams. Sound and Sources of Sound. Ellis Horwood, 1983.

3   J. W. S. Rayleigh. The theory of sound Vol. II. New York: Dover, 1945.

4   T. Lieuwen, H. Torres, C. Johnson, and B. T. Zinn. A mechanism of combustion instability in lean premixed gas turbine combustors. Journal of Engineering for Gas Turbines and Power, 123(1):182-189, 2001.

5   K. R. McManus, T. Poinsot, and S. M. Candel. A review of active control of combustion instabilities. Progress in energy and combustion science, 19(1):1-29, 1993.

6   S. J. Illingworth, A. S. Morgans, and C. W. Rowley. Feedback control of flow resonances using balanced reduced-order models. Journal of Sound and Vibration, 330(8):1567-1581, 2011.

7   A. S. Morgans and A. P. Dowling. Model-based control of combustion instabilities. Journal of Sound and Vibration, 299(1):261-282, 2007.

8   H. C. Mongia, T. J. Held, G. C. Hsiao, and R. P. Pandalai. Challenges and progress in controlling dynamics in gas turbine combustors. Journal of Propulsion and Power, 19(5):822-29, 2003.

9   J. M. Cohen and A. Banaszuk. Factors affecting the control of unstable combustors. Journal of propulsion and power, 19(5):811-821, 2003.

10   S. M. Candel. Combustion dynamics and control: progress and challenges. Proceedings of the Combustion Institute, 29(1):1-28, 2002.

11   W. Polifke. Thermoacoustic system modelling and stability analysis: conventional approaches. In Workshop on Advanced Instability Methods, IIT Madras, Chennai, India, 2009.

12   T. C. Lieuwen. Unsteady Combustor Physics. Cambridge University Press, 2012.

13   T. C. Lieuwen. Modeling premixed combustion-acoustic wave interactions: A review. Journal of Propulsion and Power, 19(5):765-781, 2003.

14   Y. Huang and V. Yang. Dynamics and stability of lean-premixed swirlstabilized combustion. Progress in Energy and Combustion Science, 35(4):293-364, 2009.

15   A. A. Putnam and W. R. Dennis. Survey of organ-pipe oscillations in combustion systems. The Journal of the Acoustical Society of America, 28:246, 1956.

16   B. T. Chu and L. S. G. Kovasznay. Non-linear interactions in a viscous heat-conducting compressible gas. Journal of Fluid Mechanics, 3:494-514, 1958.

17   F. Nicoud and T. Poinsot. Thermoacoustic instabilities: Should the rayleigh criterion be extended to include entropy changes? Combustion and Flame, 142(1):153-159, 2005.

18   F. E. C. Culick. Combustion instabilities in liquid-fueled propulsion systems, paper no. 1. In AGARD Conference Proceedings, number 450, 1988

19   B. T. Zinn. A theoretical study of nonlinear combustion instability in liquidpropellant rocket engines. AIAA journal, 6(10):1966-1972, 1968.

20   F. E. C. Culick. Nonlinear behaviour of acoustic waves in combustion chambers - 1. Acta Astronautica, 3(9-10):715 - 734, 1976.

21   J. N. Levine and J. D. Baum. A numerical study of nonlinear instability phenomena in solid rocketmotors. AIAA Journal, 21(4):557-564, 1983.

22   Compositional inhomogeneities as a source of indirect combustion noise L Magri, J O'Brien, M Ihme - Journal of Fluid Mechanics, 2016

23   F. E. Marble and S. M. Candel. Acoustic disturbance from gas nonuniformities convected through a nozzle. Journal of Sound and Vibration, 55(2):225-243, 1977.

24   T. C. Lieuwen, V. Yang, and F. K. Lu. Combustion instabilities in gas turbine engines: operational experience, fundamental mechanisms and modeling. American Institute of Aeronautics and Astronautics, 2005.

25   B. D. Bellows. Characterization of nonlinear heat release-acoustic interactions in gas turbine combustors. PhD thesis, Georgia Institute of Technology, 2006.

26   S. Hemchandra. Dyamics of turbulent premixed flames in acoustic fields. PhD thesis, Georgia Institute of Technology, 2009.

27   A. P. Dowling. Nonlinear self-excited oscillations of a ducted flame. Journal of Fluid Mechanics, 346(1):271-290, 1997.

28   A. P. Kelley and C. K. Law. Nonlinear effects in the extraction of laminar flame speeds from expanding spherical flames. Combustion and Flame, 156(9):1844-1851, 2009.

29   N. Karimi, M. J. Brear, S.-H. Jin, and J. P. Monty. Linear and non-linear forced response of a conical, ducted, laminar premixed flame. Combustion and Flame, 156(11):2201 - 2212, 2009.

30   T. Schuller, D. Durox, and S. Candel. A unified model for the prediction of laminar flame transfer functions: comparisons between conical and v-flame

31   dynamics. Combustion and Flame, 134(1-2):21 - 34, 2003.

32   Shreekrishna, S. Hemchandra, and T. Lieuwen. Premixed flame response to equi-
        valence ratio perturbations. Combustion Theory and Modelling, 14(5):681-714,
        2010.

33   E. Kalnay, Baxter, R. Hastings, N. Law, A. Glass, E. J. Atmospheric modelling,
        data assimilation and predictability, 2008.

34   Kalnay, E., M. Kanamitsu, R. Kistler, W. Collins, D. Deaven, L. Gandin, M. Iredell,
        S. Saha, G. White, J. Woollen, Y. Zhu, M. Chelliah, W. Ebisuzaki, W. Higgins, J.
        Janowiak, K. C. Mo, C. Ropelewski, J. Wang, A. Leetmaa, R. Reynolds, R. Jenne,
        and D. Joseph, 1996: The NCEP/NCAR 40-year Reanalysis Project. Bull. Amer.
        Meteor. Soc. 77, 437-471.

35   G. Evensen. Data Assimilation - The Ensemble Kalman Filter (Second Edition)
        2009

36   Matthew P. Juniper. Triggering in the horizontal Rijke tube: Non-normality, tran-
        sient growth and bypass transition. Journal of Fluid Mechanics, 667:272-308,
        2011.

37   Matthew P. Juniper and R.I. Sujith. Sensitivity and Nonlinearity of Thermoacoustic
        Oscillations. Annual Review of Fluid Mechanics, 50(1):661-689, 2018. ISSN
        0066-4189. doi: 10.1146.

38   Balasubramanian, K. & Sujith, R. I. 2008a Thermoacoustic instability in a Rijke
        tube: nonnormality and nonlinearity. Phys. Fluids 20, 044103.

39   Heckl, M. 1990 Nonlinear acoustic effects in the Rijke tube. Acustica 72, 63.

40   Dowling, A. P. 1997 Nonlinear self-excited oscillations of a ducted flame. J. Fluid
        Mech. 346, 271–290.

41   Dowling, A. P. 1999 A kinematic model of a ducted flame. J. Fluid Mech. 394,
        51–72.

42   Noiray, N., Durox, D., Schuller, T. and Candel, S. M. 2008 A unified framework for nonlinear combustion instability analysis based on the flame describing function. J. Fluid Mech. 615, 139–167.

43   Landau and Lifshitz. Fluid Mechanics 2nd Edition : Course of Theoretical Physics, Volume 6.

44   William H. Press, Saul A. Teukolsky, William T. Vetterling, Brian P. Flannery. Numerical Recipes 3rd Edition: The Art of Scientific Computing, 2007.

45   Paolo Luchini and Alessandro Bottaro. Adjoint Equations in Stability Analysis. Annual Review of Fluid Mechanics, 46(1):493-517, 2014.

46   Magri, L., Adjoint methods as design tools in thermoacoustics, Applied Mechanics Reviews, under review.

47   Lorenz, Edward Norton (1963). "Deterministic nonperiodic flow". Journal of the Atmospheric Sciences. 20 (2): 130–141.